AFRL-VA-WP-TR-2000-3033

AIRCRAFT DYNAMIC LOAD ALLEVIATION USING SMART ACTUATION SYSTEM

K. APPA
J. AUSMAN

APPA TECHNOLOGY INITIATIVES
22242 ANTHONY DRIVE
LAKE FOREST, CA 92630

N.S. KHOT

AIR VEHICLES DIRECTORATE (AFRL/VASD)
AIR FORCE RESEARCH LABORATORY
AIR FORCE MATERIEL COMMAND
WRIGHT-PATTERSON AFB, OH 45433-7542

M.J. BRENNER

NATIONAL AERONAUTICS AND SPACE ADMINISTRATION
DRYDEN FLIGHT RESEARCH CENTER
EDWARDS, CA 93523-0273

MARCH 2000

FINAL REPORT FOR 06/06/1999 – 03/01/2000

THIS IS A SMALL BUSINESS INNOVATION RESEARCH (SBIR) PHASE I REPORT.

AIR VEHICLES DIRECTORATE
AIR FORCE RESEARCH LABORATORY
AIR FORCE MATERIEL COMMAND
WRIGHT-PATTERSON AIR FORCE BASE OH 45433-7542

DTIC QUALITY INSPECTED 4

20000830 153

NOTICE

WHEN GOVERNMENT DRAWINGS, SPECIFICATIONS, OR OTHER DATA ARE USED FOR ANY PURPOSE OTHER THAN IN CONNECTION WITH DEFINITE GOVERNMENT RELATED PROCUREMENT, THE UNITED STATES GOVERNMENT INCURS NO RESPONSIBILITY OR ANY OBLIGATION WHATSOEVER. THE FACT THAT THE GOVERNMENT MAY HAVE FORMULATED OR IN ANY WAY SUPPLIED THE SAID DRAWING, SPECIFICATIONS, OR OTHER DATA, IS NOT TO BE REGARDED BY IMPLICATIONS, OR OTHERWISE IN ANY MANNER CONSTRUED, AS LICENSING THE HOLDER, OR ANY OTHER PERSON OR CORPORATION; OR AS CONVEYING ANY RIGHTS OR PERMISSION TO MANUFACTURE, USE, OR SELL ANY PATENTED INVENTION THAT MAY IN ANY WAY BE RELATED THERETO.

THE REPORT IS RELEASEABLE TO THE NATIONAL TECHNICAL INFORMATION SERVICE (NITS), AT NTIS IT WILL BE AVAILABLE TO THE GENERAL PUBLIC, INCLUDING FOREIGN NATION.

THIS TECHNICAL REPORT HAS BEEN REVIEWED AND IS APPROVED FOR PUBLICATION.

Narendra S. Khot
Project Engineer
Structural Design and Development Branch
Structures Division
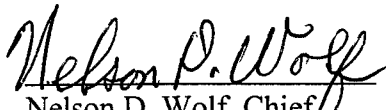
Nelson D. Wolf, Chief
Structural Design and Development Branch
Structures Division
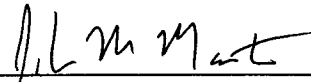
JOSEPH M. MANTER
Chief
Structures Division

IF YOUR ADDRESS HAS CHANGED, IF YOU WISH TO BE REMOVED FROM OUR MAILING LIST, OR IF THE ADDRESSEE IS NO LONGER EMPLOYED BY YOUR ORGANIZATION, PLEASE NOTIFY AFRL/VASD 146, 2210 8TH STREET, WPAFB OH 45433-7531

REPORT DOCUMENTATION PAGE

1. AGENCY USE ONLY *(Leave blank)*	2. REPORT DATE	3. REPORT TYPE AND DATES COVERED
	MARCH 2000	FINAL REPORT FOR 06/06/1999 - 03/01/2000

4. TITLE AND SUBTITLE
AIRCRAFT DYNAMIC LOAD ALLEVIATION USING A SMART ACTUATION SYSTEM

5. FUNDING NUMBERS
C   F33615-99-C-3214
PE   65502
PR   2401
TA   55
WU   00

6. AUTHOR(S)
K. APPA, J. AUSMAN -- Appa Technology Initiatives
N.S. KHOT -- AFRL/VASD
M.J. BRENNER -- National Aeronautics and Space Administration

7. PERFORMING ORGANIZATION NAME(S) AND ADDRESS(ES)
APPA TECHNOLOGY INITIATIVES
22242 ANTHONY DRIVE
LAKE FOREST, CA 92630

8. PERFORMING ORGANIZATION REPORT NUMBER

9. SPONSORING/MONITORING AGENCY NAME(S) AND ADDRESS(ES)
AIR VEHICLES DIRECTORATE
AIR FORCE RESEARCH LABORATORY
AIR FORCE MATERIEL COMMAND
WRIGHT-PATTERSON AFB, OH 45433-7542
POC: N.S. KHOT, AFRL/VASD, 937-255-8474

10. SPONSORING/MONITORING AGENCY REPORT NUMBER
AFRL-VA-WP-TR-2000-3033

11. SUPPLEMENTARY NOTES
THIS IS SMALL BUSINESS INNOVATION RESEARCH (SBIR) PHASE I REPORT.

12a. DISTRIBUTION AVAILABILITY STATEMENT
APPROVED FOR PUBLIC RELEASE; DISTRIBUTION UNLIMITED.

12b. DISTRIBUTION CODE

13. ABSTRACT *(Maximum 200 words)*

This report was developed under SBIR contract for topic AF99-280 describes an analytical development of buffet and gust load alleviation methodology. An active control surface modal device is employed to generate out-of-phase aerodynamic damping that reduces dynamic loads arising from buffet and gust encounter. Lightweight smart actuators having high response rate are used to activate the control surface modal device. This concept can also be applied to flutter suppression of any lifting surfaces. This active control algorithm can be implemented and operated independently of the primary flight control systems to avoid interference. The test cases include buffeting of F-18 twin vertical tails in high alpha flight configuration and gust environment. Analytical predictions show 80 percent reduction in tail root stress that could result in eight fold increase in fatigue life of an aircraft. Consequently, if this dynamic load alleviation methodology is implemented into existing and new military aircraft several millions of dollars can be saved per aircraft in its service life.

14. SUBJECT TERMS
SBIR Report, Smart Actuation System, Feasibility Study, Optimal Control, Aircraft Maneuver

15. NUMBER OF PAGES
72

16. PRICE CODE

17. SECURITY CLASSIFICATION OF REPORT	18. SECURITY CLASSIFICATION OF THIS PAGE	19. SECURITY CLASSIFICATION OF ABSTRACT	20. LIMITATION OF ABSTRACT
UNCLASSIFIED	UNCLASSIFIED	UNCLASSIFIED	SAR

TABLE OF CONTENTS

PREFACE

An active control surface modal device is employed to generate out-of-phase aerodynamic damping and to reduce dynamical loads arising from buffet and gust encounter. This concept can also be applied to flutter suppression of any lifting surface. A theoretical discussion describing the buffet and gust load alleviation methodology is presented. The algorithm uses the commercial MATLAB platform to perform the test cases. The test cases include buffeting of F-18 twin vertical tails in high alpha flight configuration and gust environment. Analytical predictions show an 80 percent reduction in tail root stresses and nearly an eight fold increase in fatigue life.

1 INTRODUCTION

Civil and military aircraft encounter a number of dynamic load conditions that result from fluctuating air loads. Such an environment leads to ride discomfort, structural fatigue damage, and flight performance degradation. Buffet is a turbulent air flow phenomenon that originates from the flow-separated wake behind aerodynamic lifting surfaces or bodies. A typical example, shown in Figure 1-1, depicts the release of strong vortices behind the leading edge extension of an aircraft in a high alpha maneuvering flight condition. At some distance from its origin, the vortex core becomes unstable and busts, engulfing the twin tails. Thus, the micro vortices generate fluctuating pressure field of random nature and excite the tails very severely.
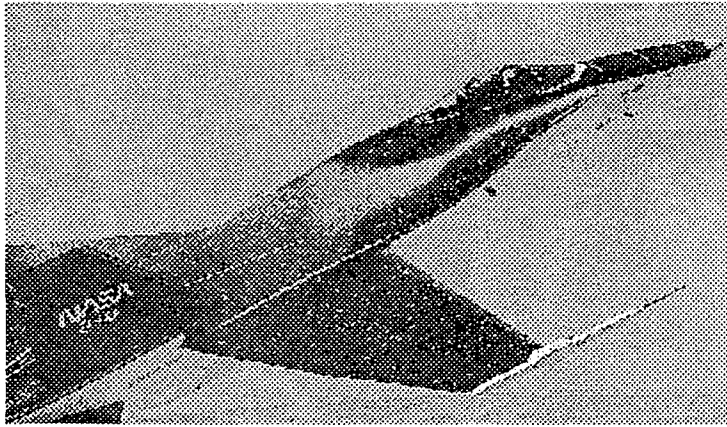
**Figure 1-1. Origination of Vortex at the Intersection of the
Fuselage and The Leading Edge Extension (Reference1)**

Such dynamic environments have caused fatigue failures at the root and midsections of the vertical tails. Sometimes, tail skin fasteners around the rudder hinge line are seen to have disappeared. Buffet-induced excitation can also lead to dynamic problems of an engine mount that is close to the tail root section. Specifically, high performance aircraft, such as the F-14, F-15, F-18, and F-22 (Ref. 2), that have twin vertical tails have experienced sever fatigue damage and increased life cycle cost. Buffeting problems are also anticipated in the case of single-finned aircraft such as the European EFA and the French Rafael.

Therefore, buffet load problems have been extensively studied by a number of investigators (e.g. References 1 through 11). These studies were conducted in two parts. The first part of the study was devoted to the understanding of the physical characteristics of the fluctuating pressures, while the second part was focused on the remedial procedures. The remedial procedures consist of passive and active control methods. A brief account of these studies is presented next.

1.1 Passive Buffet Load Control Methods

The passive methods include various configurations of the leading edge extension (LEX) with and without fences on the LEX (e.g. Refs. 3 and 4). The fences break up the vortex core and

consequently reduce the vortex strength. However, strong vortex cores are required to generate suction pressure to achieve super-maneuverability. Although fences can reduce the root bending moment on the vertical tails, these were not recommended for implementation in the production series for two reasons: (1) they are expensive to install, and (2) they degrade the flow quality that is intended for high alpha maneuvers. Reference 5 reports an alternate passive method that uses blowing and suction of air around LEX to suppress buffeting.

1.2   Active Buffet Load Control Methods

Two different active control methods are used to reduce the buffet loads.

The first principle uses aerodynamic effectors (control surfaces) to generate aerodynamic damping that reduces buffet-induced oscillations. The deployment of these effectors is achieved by means of actuators, either of conventional hydraulic actuators that function in low frequency bandwidth or the smart actuators that function in broad band frequency range. The power requirement is directly related to the amount of damping required, or in other words, deployment amplitude of the effectors. This approach provides a positively superior dynamic load control.

The second principle uses an anti-wave generation method in which the structure is excited out-of-phase of its natural frequencies with the forcing signals. In this approach, cancellation can be achieved only at discrete frequencies of the structural modes. At other frequencies, enormous power is required to excite the structure in anti-wave mode. Since buffet is a broad band phenomenon, it can force all structural modes at the same time. However, the wave cancellation method can be effective only at one frequency at a time. This is the principle used in the surface mounted piezoactuators. Therefore, the surface mounted actuator device is considered to be inefficient.

Holt Ashley and his associates (Ref. 6) used the first principle to reduce the buffet induced structural stresses. They oscillated the rudder by means of conventional hydraulic or pneumatic actuators to generate out-of-phase unsteady aerodynamic loads to suppress the vibration of the tail. This study showed a 30% reduction in the tail root bending moment. However, there are two main problems in this approach. The first problem is that the flight control system and the buffet load control system use the same control surface, which reduces the availability of the control surface for either purpose. Moreover, the interference of the active load control with the flight control is an undesirable aspect, which the pilots would like to avoid. The second drawback of this approach is that the conventional actuators are limited in the frequency bandwidth. This is because it is difficult to oscillate a massive rudder (e.g. F/A-18 rudder weighs about 64 lbs.) at higher frequencies about its hinge line. Hence, its ability to function in a wide-band spectrum of buffet load is limited.

A wind tunnel study sponsored by NASA under the ACROBAT program (Ref.7) reported a 60% reduction in the buffet-induced bending moment. This wind tunnel study employed a 1/6-scale F-18 model with actively-controlled surface-mounted piezoelectric actuators on the vertical fins. The disadvantage of this approach will be discussed shortly.

Another study currently in progress is under the auspices of the International Follow-On Structural Test Program (IFOSTP) funded by the US Air Force with the primary objective to control the buffet loads on the F-18 vertical tails. Surface-mounted actively-controlled

piezoelectric actuators are used in this investigation. The ground vibration tests have been completed and flight tests are yet to be conducted. No written document of this study exists.

The surface mounted piezoelectric actuators proposed in the above mentioned programs are good candidates for wind tunnel models, but have no practical value for the production-scale aircraft because of the following reasons:

- The surface-mounted piezoelectric actuators cannot produce anti-modal waves to oppose buffet excitation, nor withstand large surface strains.

- The wind tunnel model studies assumed that actively-controlled piezoelectric actuators provide necessary mechanical damping to suppress vibration. This assumption does not hold good for full-scale aircraft. In reality, aerodynamic damping plays a greater role than the mechanical damping. The merits of aerodynamic damping have been well demonstrated in active flutter suppression technologies.

- Surface-mounted actuators and electrical contacts may fail due to fatigue and erosion.

- Surface-mounted actuators can cause flow separation.

- There is a weight penalty if the surface-mounted actuators are used in large quantities.

- High voltage input will be required, which could cause the risk of arcing across structural joints.

Still another study (Ref. 12) reports a buffet load alleviation methodology by means of blowing high momentum fluid into the vortex core. Although lift increments have been observed in earlier experimental studies, vortex burst cannot be avoided. Hence, twin-tails are not guaranteed to be free from buffet-induced vibrations. In general, a near field active control device is a better insurance against undesirable disturbances than a far field blowing method reported in Reference 5. Moreover, the buffet load prediction method that uses a conventional computational fluid dynamics (CFD) implicit integration algorithm (Ref. 12) can't capture the stochastic phenomena of microscopic fluid particles.

In addition to buffet, the gust environment is another important aspect of aircraft dynamic load criteria that arises from atmospheric turbulence. When an aircraft penetrates a sinusoidal gust wave, the vertical lift either increases or decreases, depending on the direction of the gust velocity vector. Thus, an aircraft will be subjected to external excitations leading to ride discomfort and structural fatigue damage. Still another design criterion that requires careful consideration is the flutter aeroelastic instability. Flutter is a self-excited oscillatory phenomenon that results in structural instability, leading to catastrophic destruction when the flight speed exceeds the design speed limit. Hence, there is a need to remedy these problems to ensure structural stability, reliability, and enhanced fatigue life.

The present investigation relates to an "Active Control Surface Modal (ACSM)" device that generates unsteady aerodynamic damping to alleviate aeroelastic structural instability, vibration and dynamic loads. An active control surface modal deformation is created by means of a pair of antagonistically activated actuators. The light weight upper and lower surface skins can be activated at high frequencies that encompass the wide band spectrum of buffet, gust and self excited flutter phenomena. An independent closed loop active control system is employed to activate the ACSM modes. Measured acceleration sensors are used as the feedback signals to compute the coefficients of the control law that are designed to suppress the dynamic environment such as buffet, gust and flutter. Then a computerized control system

3

algorithm outputs a series of voltage signals that pass through a power amplifier that activates the actuators. Thus, the ACSM device generates unsteady aerodynamic damping in out-of-phase with the external (buffet/gust) or self-excited air loads (flutter) to reduce or eliminate the undesirable dynamic effects on the aircraft. Preliminary buffet analyses show 60 to 80 percent reduction in peak stress, which amounts to an eight fold fatigue life enhancement of the vertical tails. This improvement could save millions of dollars during the service life of an aircraft.

2 ANALYTICAL MODELING OF AIRCRAFT DYNAMICS

2.1 An Overview

The main objective of this study is to develop an analytical method to demonstrate the proof-of-concept of buffet load alleviation using a smart actuation system. The F-18 vertical tail configuration was selected as the benchmark case to verify the proposed concept. The rudder of the vertical tail was fitted with a smart actuation system, a derivative of the prior art covered under the U.S. Patent Number 5,887,828. A typical example is shown in Figure 2-1. The actuator pairs deform the rudder uniformly either upward or downward according to signals commanded by an active control system.
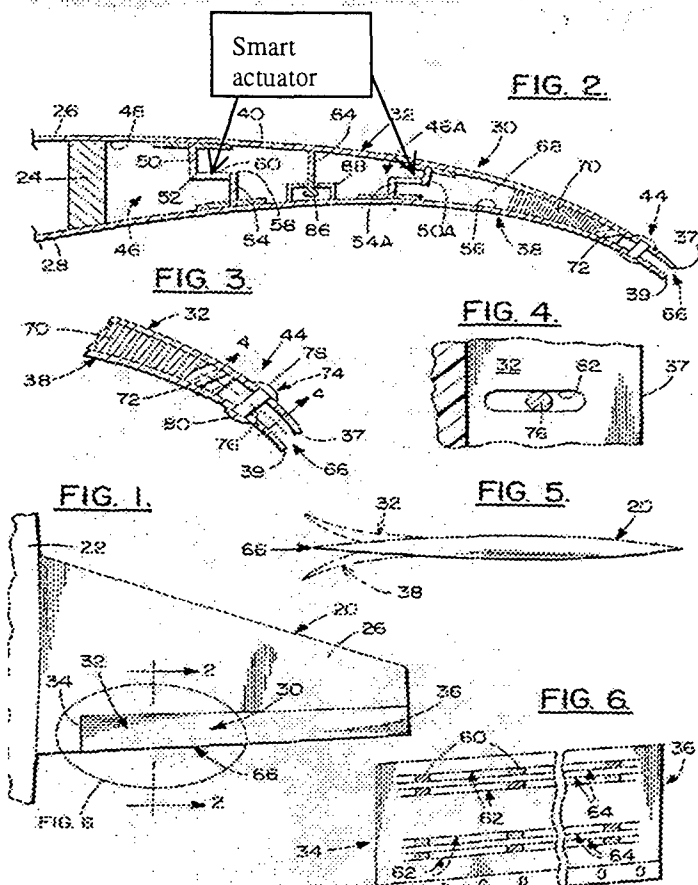
Figure 2-1. A Smart Aerodynamic Effector Actuation System
(U.S. Patent No: 5,887,828)

Unlike the hydraulic or pneumatic actuators, the smart actuators respond rapidly to a signal. Hence, an Active Control Surface Modal (ACSM) device is developed to generate the necessary aerodynamic damping in a wide range of frequency spectrum. Since buffet is a broadband load environment, the ACSM device can alleviate the resulting dynamic loads very

5

effectively. Likewise, the gust load environment can also be minimized. Further, the ACSM device can be used to suppress flutter, a self-excited aeroelastic instability phenomena. The mathematical details of the approach are presented in the following sections. The mathematical modeling of the ACSM device is presented in this section.

2.2 Aircraft Dynamics

The life expectancy of aircraft components requires accurate computation of peak stress levels and the corresponding cycles. Therefore, the dynamic analysis must include the computation of maneuver loads as the basic requirement. The following discussion presents a generalized set of equations of motion pertaining to flexible aircraft in dynamic environments. However, the final solution, within the scope of this study will be limited to the aspects of buffet load alleviation using an actively controlled smart actuation system.

2.2.1 Equations of Motion

The equations of motion of a maneuvering flexible aircraft can be written as:

$$Kr + C\dot{r} + M\ddot{r} + QT^T A_S \alpha + QT^T A_u(\kappa)r_a + F_u u + F_b + F_{external} = 0 \qquad (2\text{-}1)$$

where

α = A vector of angles of attack at the centers of aerodynamic panels

A_S = Steady Aerodynamic Influence Coefficients (AIC) matrix with respect to aerodynamic panels

F_u = A matrix of nodal forces due to actuator elements

K = A structural stiffness matrix in structural degrees of freedom (DOF)

M = A mass matrix

r_a = A displacement vector at aerodynamic panel centers

r = A displacement vector in structural dof

T = A transformation matrix relating structural dof to aerodynamic dof

u = A vector of actuator stimuli (input in volt)

A_u = Motion dependent unsteady Aerodynamic Influence Coefficient (AIC) matrix for reduced frequency κ

F_b = A body force vector due to gravitational and centripetal accelerations

$F_{external}$ External load vector resulting from gust, buffet and/or acoustic environment

$$Q \qquad = \text{Dynamic pressure, } \rho V^2 / 2$$

$$C \qquad = \text{A structural damping matrix}$$

$$\kappa \qquad = \text{Reduced frequency, } (\omega l / V) > 0$$

The structural displacement vector, r, can be expressed as a linear combination of rigid body modes, vibration modes and control surface deformation modes.

Thus, we have:

$$r = [\psi_r \psi_e \psi_c] \begin{Bmatrix} \eta_r \\ \eta_e \\ \eta_c \end{Bmatrix} = [\psi] \eta \qquad \text{(2-2a)}$$

$$r_a = T^T r = T^T \psi \eta = \psi_a \eta \qquad \text{(2-2b)}$$

$$= \text{displacement at the aerodynamic panel centers}$$

In which:

$\psi_r \qquad = \quad$ A matrix of rigid body modes such as plunge (Z), sideslip (Y), pitch (θ), roll (ϕ), and yaw (ψ). The control surface rotation modes may also be adjoined to represent conventional aerodynamic effectors if desired.

$\psi_e \qquad = \quad$ A matrix of vibration modes (including symmetric and antisymmetric components)

$\psi_a \qquad = \quad$ A transformation matrix in aerodynamic dof

$\psi_c \qquad = \quad$ A control surface deformation modal matrix due to the generalized actuator forces

$\eta \qquad = \quad \{\eta_r \, \eta_e \, \eta_c\} \quad$ a vector of generalized coordinates

The subscript 'r' denotes the rigid body modes, 'e' denotes the elastic vibration modes and 'c' represents the control actuator modes.

The angle of attack (incidence) at the center of each aerodynamic panel is given by:

$$\alpha = T \frac{\dot{r}}{V} = \frac{1}{V} T [\frac{\partial r}{\partial t} + U . \nabla r] = \frac{1}{V} T [\psi \dot{\eta} + u \frac{\partial \psi}{\partial x} \eta] \qquad \text{(2-3a)}$$

or:

$$\alpha = \overline{\psi} \dot{\eta} + \psi_x \eta \qquad \text{(2-3b)}$$

where:

$$\overline{\psi} = \frac{1}{V} T \psi,$$

(2-3c)

$$\psi_x = T \frac{\partial \psi}{\partial X}$$

(2-3d)

and:

V   =   is the free stream velocity

u   =   is the chordwise component of V

η_r = $\{Z, Y, \phi, \theta, \psi\}$ is a vector of generalized rigid body coordinates

$\dot{\eta}_r$ = $\{\dot{Z}, \dot{Y}, p, q, r\}$, is the corresponding velocity vector in rigid body motion

The rigid body motion in the flight direction (x) has been omitted since the computation of drag is not accurate in the linear aerodynamic methods. Should accurate drag computation tools become available, then all six degrees of freedom in the rigid body modes may be included in the analytical model.

From equation (2-3b), the rigid body angle of incidence and side slip angle are given by:

$$\alpha_i = \theta - \frac{\dot{Z}}{V}, \beta_i = -\frac{\dot{Y}}{V}$$

(2-4)

2.3   Computation of the Control Surface Modal Matrix

A pair of actuator forces acting in opposite directions is used to denote a system of generalized force. The deformed shape of the lifting surface for a unit value of this force denotes the control surface mode. Figure 2-2 shows a schematic arrangement of the pair of actuators.

For each pair of actuators, it is assumed that a unit force is being applied: one force +1, other force −1.0. The unit actuator load is being reacted equally at each end. Then, the unit force is resolved into the three component loads. Let Nx, Ny, Nz be the direction cosines of the centerline of the upper actuator, and similarly assume Mx, My, Mz be the direction cosines of lower actuator. Let N1, N2, N3 and N4 be the row location numbers of the actuator nodes 1, 2, 3, and 4, respectively. The corresponding load vector for a unit value of axial force in actuator i, is given by Equation 2-5a.

8

$$\overline{F}_{ui} = \begin{Bmatrix} N1:Nx \\ Ny \\ Nz \\ 0 \\ 0 \\ 0 \\ \cdot \\ \cdot \\ \cdot \\ N2:-Nx \\ -Ny \\ -Nz \\ 0 \\ 0 \\ 0 \\ \cdot \\ N3:-Mx \\ -My \\ -Mz \\ 0 \\ 0 \\ 0 \\ 0 \\ \cdot \\ N4:Mx \\ My \\ Mz \\ 0 \\ 0 \\ 0 \\ \cdot \end{Bmatrix}$$

(2-5a)
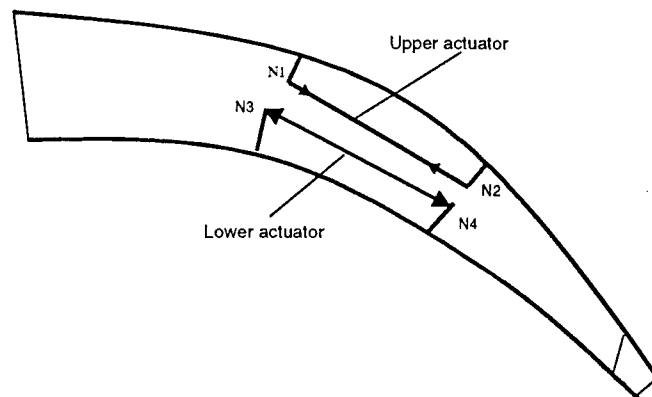
Figure 2-2. A Typical System of Generalized Actuator Forces

Next, adjoining the load vectors for all actuator sets i=1... n_a:

$$\overline{F}_u = [\overline{F}_{u1} \quad \overline{F}_{u2} \quad . \quad . \qquad \overline{F}_{una}] \qquad (2\text{-}5b)$$

Then, the load vector is given by:

$$F_u = \overline{F}_u \, D \qquad (2\text{-}5c)$$

In which D denotes a diagonal matrix of axial forces in each pair of actuator.

Then, the actuator activated control surface deformation matrix is given by:

$$[\phi_C] = [K_{gg}]^{-1}[\overline{F}_u] \qquad (2\text{-}6)$$

In which K_{gg} denotes stiffness matrix of the rudder. After computing the rigid body and the vibration modes using the ASTROS software, the last n_a columns of vibration modes will be replaced by the $[\phi_c D]$ matrix as defined by equation (2-7).

$$\Phi_g = [\phi_r \quad \phi_e \quad \phi_c D] \qquad (2\text{-}7)$$

2.4   External Load Vector Due to the Gust Environment

Generally two types of gust load environments are used in aircraft design. For sake of simplicity, discrete gust load factors were used in earlier designs. A more refined approach uses the so-called "one-minus- cosine" gust model. However, with the development of high speed aircraft with increased flexibility, gust loads were found to produce significant dynamic responses giving rise to sever load conditions. Therefore, investigators and designers turned to power spectral techniques to compute realistic design loads. The gust and buffet load data are presented in the form of power spectral densities and root mean square values (RMS). This data can be used to compute the corresponding response characteristics: either the accelerations or the stresses of aircraft. However, to conduct load alleviation studies using active control laws, the spectral data must be transformed to time history data as discussed later.

The gust load vector can be written as:

$$F_{gust} = [QT^T A_u e^{-i\theta} e^{i\Omega a}](w_g / V) = F_g \alpha_g \qquad (2\text{-}8)$$

where:

$\Omega = (\omega / V)$ = Spatial frequency in radians per foot

$\theta = (\omega x / V)$ = Phase angle delay at each panel with respect to a reference point

a = Initial point of gust encounter

Ωa = Initial gust orientation angle

$\alpha_g = (w_g / V)$ = Gust angle of incidence

10

$$V \qquad = \text{Aircraft speed}$$

The gust velocity, w_g, of a continuous turbulence model is generally expressed in terms of power spectral density (PSD), given in the following two forms:

Dryden Spectrum:

$$S_w(\Omega) = (\frac{L\sigma_w^2}{V})(\frac{1 + 3(\Omega L)^2}{(1 + (\Omega L)^2)^2}) \tag{2-9a}$$

Von Karman Spectrum:

$$S_w(\Omega) = (\frac{L\sigma_w^2}{V})(\frac{1 + (8/3)(1.339\Omega L)^2}{(1 + (1.339\Omega L)^2)^{(11/6)}}) \tag{2-9b}$$

in which

$$L \qquad = \text{turbulence scale in feet or meter}$$

and

σ_w is the RMS value of the vertical gust velocity, w_g.

The second order Dryden model of the vertical gust, in the state space representation using the Pade approximation, is given by:

$$\frac{w_g}{\eta_g} = \sigma_{wg}\sqrt{\frac{3V}{L}}(\frac{\frac{V}{\sqrt{3}L} + s}{((V/L) + s)^2}) \tag{2-10}$$

Where:

$$s = i\omega \quad = \quad \text{Laplace transform operator}$$

$$\eta_g \qquad = \quad \text{State coordinate of the gust model}$$

This form of the gust load can easily be integrated into the state space formulation.

2.5 Buffet Load Spectrum

The buffet pressure data for a specific aircraft configuration are collected either by means of wind tunnel tests or the flight test records. The data for various points on the lifting surface are presented in terms of power spectral density (e.g. p^2/Hz) vs. frequency for varying angles of attack and dynamic pressures. In this process, the phase angle information is lost. Moreover, unlike the atmospheric turbulence model, no analytical model exists for the buffet pressure data. Nevertheless, without loss of generality, randomly generated phase shift can be

assumed to transform the power spectral data into the time history data. Let a Fourier transform pair be written as:

$$X(\omega) = \int_{-\infty}^{\infty} x(t)e^{-i\omega t} dt$$

(2-11a)

$$x(t) = \int_{-\infty}^{\infty} X(\omega)e^{i\omega t} \frac{d\omega}{2\pi}$$

(2-11b)

If the data is sampled over a period of T seconds, then the relation between the power spectral density and the Fourier spectra can be written as:

$$S_x(\omega) = \frac{X(\omega)^* X(\omega)}{T} = \frac{|X(\omega)|^2}{T}$$

(2-12)

Thus, the buffet pressure time history, using the inverse Fourier transform, can be written as:

$$p(t) = \sqrt{2\Delta f} \sum_{k=1}^{k=N} \sqrt{S_{pk}(f)} e^{i(2\pi f_k t + o_k)}$$

(2-13)

where:

f_k =   Centered frequency (in Hertz) at k^{th} strip having the width $\Delta f = 1/T$

S_{pk} =   PSD of the pressure in the kth strip

ϕ_k =   Phase angle randomly generated between 0 and 2π

The computational procedure is as follows:

Select a series of random values of ϕ_k and compute real and imaginary components of the Fourier spectra of the pressure:

$$P_{Real}(f)_k = \sqrt{2\Delta f} \sqrt{S_k(f)} Cos(\phi_k)$$

$$P_{Imaginary}(f)_k = \sqrt{2\Delta f} \sqrt{S_k(f)} Sin(\phi_k)$$

(2-14)

Next, a fast Fourier transform is used to compute the pressure time history, p(t) at all known data points on the structural surface.

$$p(t) = \int_0^{f_{max}} P(f)e^{i2\pi ft} df$$

(2-15)

A typical plot of power spectral density of buffet pressure at a point on the vertical tail is shown in Figure 2-3 (Ref. 11). The corresponding pressure time history is presented in Figure 2-4.

Power Spectra, S

Frequency f
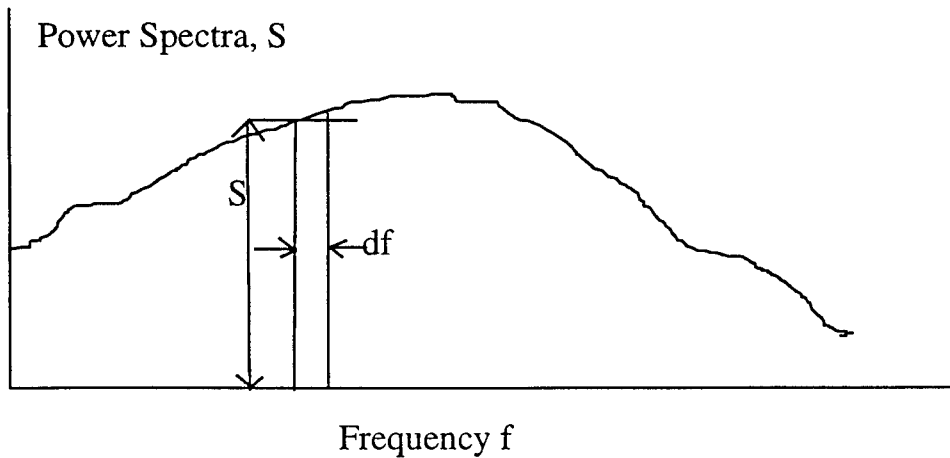
Figure 2-3. Power Spectral Density Used in Random History Generation
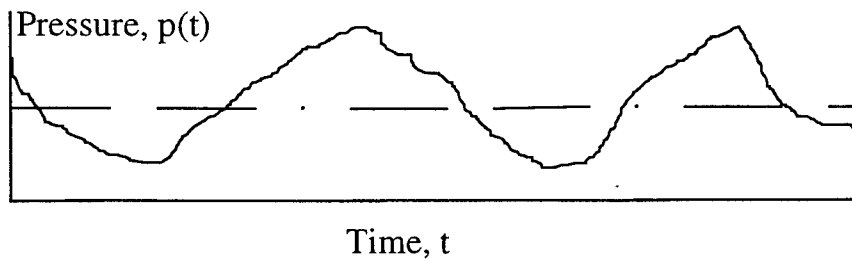
Pressure, p(t)

Time, t

Figure 2-4. Random Pressure Time History

Thus an approximate time history of the buffet pressure will be generated at known data points for each time. Then the required generalized force vector, $F_{external}$, can be computed using a known spline function to fit the pressure distribution on the lifting surface.

2.6 Aircraft Dynamics in a Generalized Coordinate System

Substituting equations (2-2a) and (2-3b) in (2-1), and pre-multiplying by ψ^T, one can rewrite the equations of motion in terms of the generalized coordinates, η:

$$\overline{K}\eta + \overline{C}\dot{\eta} + \overline{M}\ddot{\eta} + Q\overline{A}_{s1}\eta + Q\overline{A}_{s2}\dot{\eta} + Q\overline{A}_u(\kappa)\eta + \overline{F}_u u + \overline{F}_{body} + \overline{F}_{external} = 0 \qquad (2\text{-}16)$$

in which the generalized matrices are denoted by an overbar symbol. The in-phase and out-of-phase non-oscillatory air load matrices are defined by $\overline{A}_{s1}$ and $\overline{A}_{s2}$, while the oscillatory air load matrix in the frequency domain is denoted by $\overline{A}_u$. Hence, there is a need to transform the frequency spectrum data into the time domain. There are two methods to transform the unsteady aerodynamic matrix, $\overline{A}_u$, in the state space coordinates. The first approach is based on the conventional Pade approximation, while the second method uses the direct state space

13

formulation.

2.6.1 Pade Approximation

Let a truncated series expansion be given by:

$$\overline{A}_u(\kappa) = A_0 + sA_1 + s^2A_2 + (\frac{s}{\beta+s})A_3 \qquad (2\text{-}17)$$

where:

$$s = i(\frac{l}{V})\omega = i\kappa \qquad (2\text{-}18)$$

and β is the pole of the aerodynamic lag term.

Using equation (2-17) in (2-16), the dynamics of the aircraft reduces to:

$$\tilde{K}\eta + \tilde{C}\dot{\eta} + \tilde{M}\ddot{\eta} + QA_3X_a + F_u u + F_R = 0 \qquad (2\text{-}19)$$

where:

$$\tilde{K} = \overline{K} + Q\overline{A}_{s1} + QA_0 \qquad (2\text{-}20)$$

$$\tilde{C} = \overline{C} + Q\overline{A}_{s2} + Q(\frac{l}{V})A_1 \qquad (2\text{-}21)$$

$$\tilde{M} = \overline{M} + Q(\frac{l}{V})^2 A_2 \qquad (2\text{-}22)$$

$$F_R = F_{body} + F_{gust} + F_{buffet} \qquad (2\text{-}23)$$

And the aerodynamic lag coordinate is given by:

$$X_a = \frac{s}{\beta+s}\eta \qquad (2\text{-}24)$$

2.6.2 State Space Formulation

The second order differential equation (2-16) can be rewritten in terms of the first order one as shown:

$$\dot{X} + AX + Bu + F_R = 0 \qquad (2\text{-}25)$$

14

Where state vectors are given by:

$$X = \left\{ \begin{array}{c} \eta \\ \dot{\eta} \\ X_a \end{array} \right\},$$

(2-26)

$$\dot{X} = \left\{ \begin{array}{c} \dot{\eta} \\ \ddot{\eta} \\ \dot{X}_a \end{array} \right\}$$

(2-27)

and the state space matrices are defined as:

$$A = \begin{bmatrix} 0 & -I & 0 \\ \tilde{M}^{-1}\tilde{K} & \tilde{M}^{-1}\tilde{C} & Q\tilde{M}^{-1}A_3 \\ 0 & -I & (\dfrac{V}{l})\beta I \end{bmatrix},$$

(2-28)

$$B = \begin{bmatrix} 0 \\ \tilde{M}^{-1}\overline{F}_u \\ 0 \end{bmatrix},$$

(2-29)

$$F_R = \begin{bmatrix} 0 \\ \tilde{M}^{-1}\overline{F}_R \\ 0 \end{bmatrix}$$

(2-30)

in which I denotes a unit matrix.

Equation (2-25) represents a unique formulation of aircraft dynamics providing solutions to flight maneuver problems at the low end of the frequency spectrum, while at the high end of the frequency spectrum it represents the dynamics of aeroservoelastic environments.

2.6.3 Approximation of Unsteady Aerodynamic Matrix

Let the incremental data be given by:

$$A_u(\kappa) = A(\kappa) - A(0)$$

(2-31)

Then the expansion can be written in the matrix notation:

$$[R][P] = \overline{A}$$

(2-32)

where:

15

$$R = \begin{bmatrix} I & 0 & -\kappa_1^2 I & \dfrac{\kappa_1^2}{\beta^2 + \kappa_1^2} \\[2ex] 0 & I & 0 & \dfrac{\beta}{\beta^2 + \kappa_1^2} \\[2ex] I & 0 & -\kappa_2^2 I & \dfrac{\kappa_2^2}{\beta^2 + \kappa_2^2} \\[2ex] 0 & I & 0 & \dfrac{\beta}{\beta^2 + \kappa_2^2} \\[2ex] I & 0 & -\kappa_3^2 I & \dfrac{\kappa_3^2}{\beta^2 + \kappa_3^2} \\[2ex] 0 & I & 0 & \dfrac{\beta}{\beta^2 + \kappa_3^2} \end{bmatrix}$$

(2-33)

$$P = \begin{bmatrix} A_0 \\ A_1 \\ A_2 \\ A_3 \end{bmatrix}$$

(2-34)

$$\overline{A} = \begin{bmatrix} \overline{A}_{R1} \\ \overline{A}_{I1} \\ \overline{A}_{R2} \\ \overline{A}_{I2} \\ \overline{A}_{R3} \\ \overline{A}_{I3} \end{bmatrix}$$

(2-35)

For known values of $\overline{A}(\kappa)$ at a number of reduced frequencies, the AIC matrices, A_0 through A_3 can be computed from equation (2-20) by the method of least squares.

2.6.4 Direct State Formulation of Unsteady Aerodynamics

Let X_a denote the aerodynamic state vector, and f_{ua} be the unsteady air load vector. Then the aerodynamic state space matrix equation, according to Reference 13, may be given by:

$$\begin{Bmatrix} \dot{X}_a \\ f_{ua} \end{Bmatrix} = \begin{bmatrix} A_{11} & A_{12} \\ A_{21} & A_{22} \end{bmatrix} \begin{Bmatrix} X_a \\ \eta \end{Bmatrix}$$

(2-36)

16

This reduces to:

$$f_{ua} = A_u(\kappa)\eta = [A_{22} + A_{21}[sI - A_{11}]^{-1}A_{12}]\eta \qquad (2\text{-}37)$$

where

$$s = i\omega \qquad (2\text{-}38a)$$

is a Laplace operator, and:

$$X_a = [sI - A_{11}]^{-1}A_{12}\eta \qquad (2\text{-}38b)$$

Thus, the frequency domain data can be expressed in terms of four constant matrices defined in equation (2-36). These matrices can be computed using the MATLAB toolbox routines. The corresponding state matrices are given by:

$$\tilde{K} = \overline{K} + QA_{S1} + QA_{22} \qquad (2\text{-}39a)$$

$$\tilde{C} = \overline{C} + QA_{S2} \qquad (2\text{-}39b)$$

$$\tilde{M} = \overline{M} \qquad (2\text{-}39c)$$

$$\tilde{F}_R = F_{body} + F_{external} \qquad (2\text{-}39d)$$

$$A = \begin{bmatrix} 0 & -I & 0 \\ \tilde{M}^{-1}\tilde{K} & \tilde{M}^{-1}\tilde{C} & \tilde{M}^{-1}A_{21} \\ -A_{12} & 0 & -A_{11} \end{bmatrix} \qquad (2\text{-}40)$$

$$B = \begin{bmatrix} 0 \\ \tilde{M}^{-1}\overline{F}_u \\ 0 \end{bmatrix} \qquad (2\text{-}41)$$

$$F_R = \left\{ \begin{array}{c} 0 \\ \tilde{M}^{-1}\tilde{F}_R \\ 0 \end{array} \right\} \qquad (2\text{-}42)$$

2.7 Optimal Control Design

For a given set of actuator input u, equation (2-25) defines the generalized set of equations of motion of an elastic aircraft. This equation can be solved for the response characteristics of the aircraft in maneuver or transient dynamics. However in the present study, we specialize the system of equations to solve for dynamic load alleviation in buffet and gust environments. Hence, the external load vector F_R, represents a time domain data arising from either the

17

buffet load or the gust load. This problem will be solved using the optimal control theory.

Two accelerations measured at the tip section of the vertical tail are used as the required constraints. The acceleration sensor measurements are given by:

$$X_S = CX + Du \tag{2-43}$$

The corresponding constraint vector is given by:

$$\varepsilon = X_S - X_T = CX + Du - X_T \tag{2-44}$$

in which X_T represents a vector of desired target values. For example, allowable acceleration limits. Thus, the Hamiltonian function for this problem can be stated as:

$$h = \frac{1}{2}\varepsilon^T Q\varepsilon + \frac{1}{2}u^T Ru + \lambda^T(AX + Bu + F_R) \tag{2-45}$$

where:

A, B, F_R = are defined in equations (2-28,29,30) or (2-40,41,42)

R   a constant weighting diagonal matrix related to the actuator power

u = a vector of actuator stimuli

ε = a vector of constraint functions

Q = a diagonal state weighting matrix

λ = a vector of Lagrangian coefficients

The second term in equation (2-45) represents an objective function based on the actuator power. The main purpose of this objective function is to minimize the power input so that the actuator is not overly strained beyond its elastic limit.

2.7.1 Hamiltonian Equations of Motion

Differentiating the Hamiltonian function, h (equation 2-45), with respect to X, u, and λ, and using the principle of optimal control theory, we obtain the following two-point boundary value problem:

$$\left\{ \frac{\dot{X}}{\dot{\lambda}} \right\} = \begin{bmatrix} h_{11} & h_{12} \\ h_{21} & h_{22} \end{bmatrix} \left\{ \frac{X}{\lambda} \right\} + \left\{ \frac{F_1}{F_2} \right\} = [H]\left\{ \frac{X}{\lambda} \right\} + \left\{ \frac{F_1}{F_2} \right\} \tag{2-46}$$

together with the control input given by:

$$u = -\Re^{-1}[D^T QCX + B^T \lambda - D^T QX_T]$$ (2-47)

in which:

$$\Re = \left[R_i + D^T QD\right]$$ (2-48)

The elements of the Hamiltonian matrix, H, in equation (2-45) are given by:

$$h_{11} = A - B\Re^{-1}D^T QC$$ (2-49a)

$$h_{12} = -B\Re^{-1}B^T$$ (2-49b)

$$h_{21} = -C^T QC + (C^T QD)\Re^{-1}(C^T QD)^T$$ (2-49c)

$$h_{22} = -h_{11}^T$$ (2-49d)

$$F_1 = F_R - B\Re^{-1}D^T QX_T$$ (2-50)

$$F_2 = -C^T[Q - (D^T Q)^T \Re^{-1}(D^T Q)]X_T$$ (2-51)

2.7.2 Solution to Equations of Motion

The solution of the two-point boundary value problem stated in equation (2-46) can be written as:

$$\begin{Bmatrix} X(t_f) \\ \lambda(t_f) \end{Bmatrix} = \Phi(t_f,t)\begin{Bmatrix} X(t) \\ \lambda(t) \end{Bmatrix} + \int_t^{t_f} \Phi(t_f,\tau)\begin{Bmatrix} F_1(\tau) \\ F_2(\tau) \end{Bmatrix} d\tau$$ (2-52)

where t_f denotes the final time frame, and Φ denotes the transition matrix.

The transition matrix can be computed as follows:

Let χ and χ' be right and left eigenvectors of the Hamiltonian matrix H, and Λ is a diagonal matrix of corresponding eigenroots. Then the transition matrix is given by:

$$\Phi(t_f,t) = e^{H(t_f-t)} = \chi \exp(\Lambda(t_f - t))\chi'$$ (2-53)

The known end conditions are:

$$X(t) = X(t_0)$$ (2-54)

at $t = t_0$, the initial condition, while at the terminal condition:

19

$$\lambda(t_f) = 0 \tag{2-55}$$

One can rewrite equation (2-52) in matrix notation using the end conditions given by (2-54) and (2-55):

$$\begin{Bmatrix} X(t_f) \\ \lambda(t_f) \end{Bmatrix} = \begin{bmatrix} \Phi_{11} & \Phi_{12} \\ \Phi_{21} & \Phi_{22} \end{bmatrix} \begin{Bmatrix} X(t) \\ \lambda(t) \end{Bmatrix} + \begin{Bmatrix} f_1(t) \\ f_2(t) \end{Bmatrix} \tag{2-56}$$

Multiplying equation (2-56) by the inverse of Φ and rearranging we obtain:

$$\begin{Bmatrix} X(t) \\ \lambda(t) \end{Bmatrix} = \begin{bmatrix} \Psi_{11} & \Psi_{12} \\ \Psi_{21} & \Psi_{22} \end{bmatrix} \begin{Bmatrix} X(t_f) \\ \lambda(t_f) \end{Bmatrix} - \begin{Bmatrix} \bar{f}_1(t) \\ \bar{f}_2(t) \end{Bmatrix} \tag{2-57}$$

Using the end conditions given by (2-54) and (2-55) one obtains:

$$X(t_f) = [\Psi_{11}]^{-1}\{X(t) + \bar{f}_1\} \tag{2-58}$$

and the Lagrangian coefficient vector is given by:

$$\lambda(t) = \Psi_{21}\Psi_{11}^{-1}\{X(t)\} + \bar{f}_1\} - \bar{f}_2 \tag{2-59a}$$

$$\lambda(t) = PX(t) + s(t) \tag{2-59b}$$

in which the Riccati matrix is denoted by:

$$P = \Psi_{21}\Psi_{11}^{-1} \tag{2-60}$$

Finally the control law is given by:

$$u(t) = -\Re^{-1}[[D^T QC + B^T P]X(t) + B^T s(t) - D^T QX_T] \tag{2-61}$$

2.8   Closed Loop System

The control input can be written in the following simplified form:

$$u = KX(t) + \bar{s}(t) \tag{2-62}$$

Substituting equation (2-62) into equation (2-25) we obtain the closed loop system:

$$\dot{X} = \overline{A}X + \Im \tag{2-63}$$

where:

20

$$\overline{A} = A - BK \tag{2-64}$$

$$\mathfrak{S} = F_R - B\overline{s}(t) \tag{2-65}$$

The eigenvalues of the closed system $\overline{A}$ are supposed to be stable, assuring the aircraft to be dynamically stable. However, appropriate gain matrix coefficients, Q, must be selected so that any unstable roots that lie in the right half of Nyquist's plane move to the left-half, the stable region. The response of the aircraft, X, due to gust and/or buffet loads, and the corresponding sensor output, X_S, can be computed from (2-63). Finally, power spectral density and RMS values of X_S will be computed for two cases: (1) without active controls, and (2) with active controls. The merits of using smart active controls to reduce dynamic loads will be discussed. Figure 2-5 depicts the plant and the optimal controller diagram.
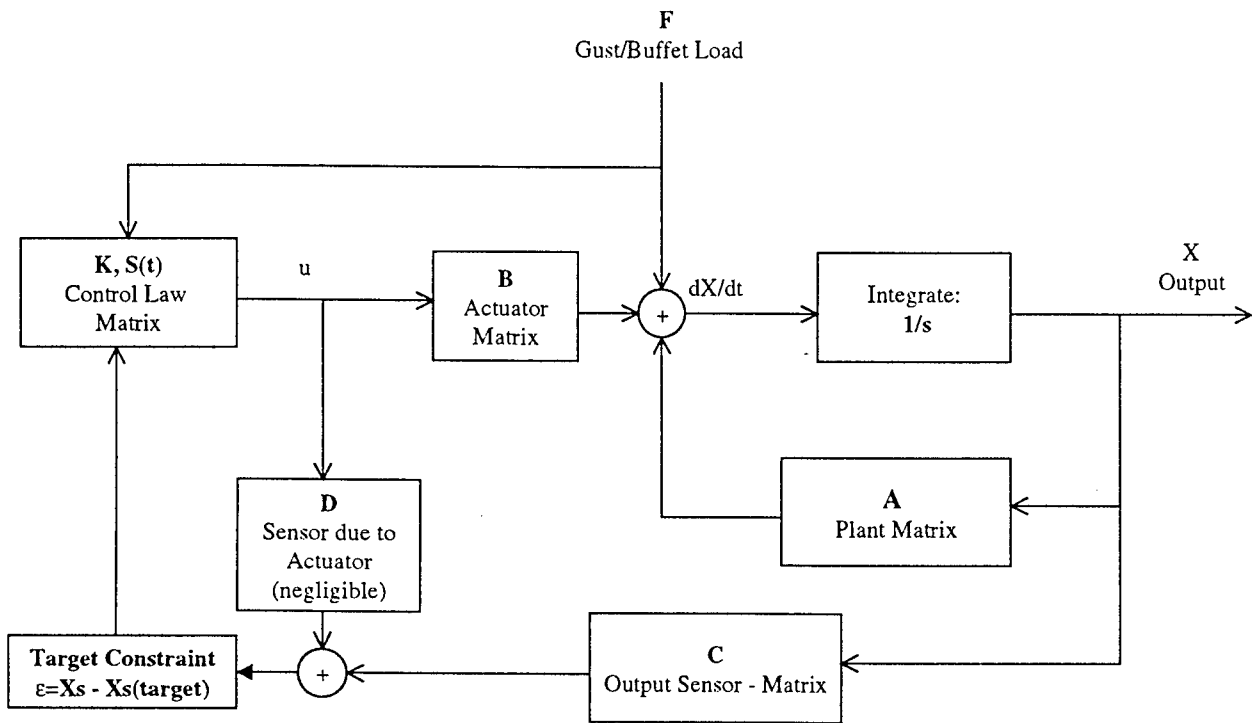
Figure 2-5. Optimal Feedback Controller Diagram

3 ACTIVE CONTROL SURFACE MODAL DEVICE

The dynamic load and stability criterion arising from buffet, gust, and flutter environments are very important design aspects required to ensure reliability and structural integrity of aircraft. Service life depends very much on the fatigue characteristics of a structure, which in turn relates to peak stresses in the dynamic environment. Buffet and gust load environments are the crucial factors that influence the design. Flutter, a self excited aeroelastic phenomena that involves structural stiffness, mass and unsteady air loads, is also an equally important design criteria. The present innovation provides a unified approach that can reduce dynamic stresses arising from buffet and gust loads, and also eliminates the phenomena of flutter within the flight envelope. Detailed description of the approach is presented in this section.

3.1 Description of the Active Control Surface Modal Device

The proposed active control surface modal (ACSM) device is an integral part of a control surface that is used to command the directional movement of an aircraft by means of a flight control system. For example, Figure 3-1 represents a typical aerodynamic lifting surface in which the dotted boundary denotes the control surface that can be used as an actively commandable aerodynamic effector. This control surface can be fitted with a number of lightweight smart actuators that can respond to high frequency signals. Generally, these are made of piezoelectric or magnetorestrictive materials. This ACSM device is a modified version of the prior art; U.S. Patent No. 5,887,828. The piezoelectric actuators produce forces in response to voltage input, while the magnetorestrictive actuators use current as the stimulant.

Figure 3-2 shows the cross-sectional view of the control surface assembly with actuator pairs attached to the inner surface of upper and lower skins. Figure 3-3 depicts the inside view of the control surface and the spanwise position of the actuator pairs. The control surface assembly is fixed to the leading edge spar. The leading edge spar is rotatably mounted on hinges H1-H2 (Fig. 3-1) so that the flight control system can use the same surface as the aerodynamic effector for trim, stabilization, or directional control of an aircraft. A composite torque tube is used to provide the necessary bending and torsion stiffness. Low-shear rigid foam-like structural materials are used to hold the upper and lower skins together and also permit relative lateral sliding motion between the upper and lower skins.

The deformed shape of the control surface can be achieved by means of antagonistic pull and push forces generated by a pair of actuators as depicted in Figure 2-2. A pair of actuators that require a single input having equal and opposite electrical potentials generates the bending action. Antagonistic amplifiers provide this type of potentials to excite a pair of actuators with opposite poles. Since the surface skin mass is relatively small, it can be actuated at high frequencies. Figures 3-4 and 3-5 show the three-dimensional view of the control surface modes generated by each pair of actuators. These modal deformations are called the "Active Control Surface Modes (ACSM)" that serve as the primary embodiment of the new concept. A linear combination of these modes produces a complex deformation and generates unsteady aerodynamic damping to suppress undesirable vibrations.
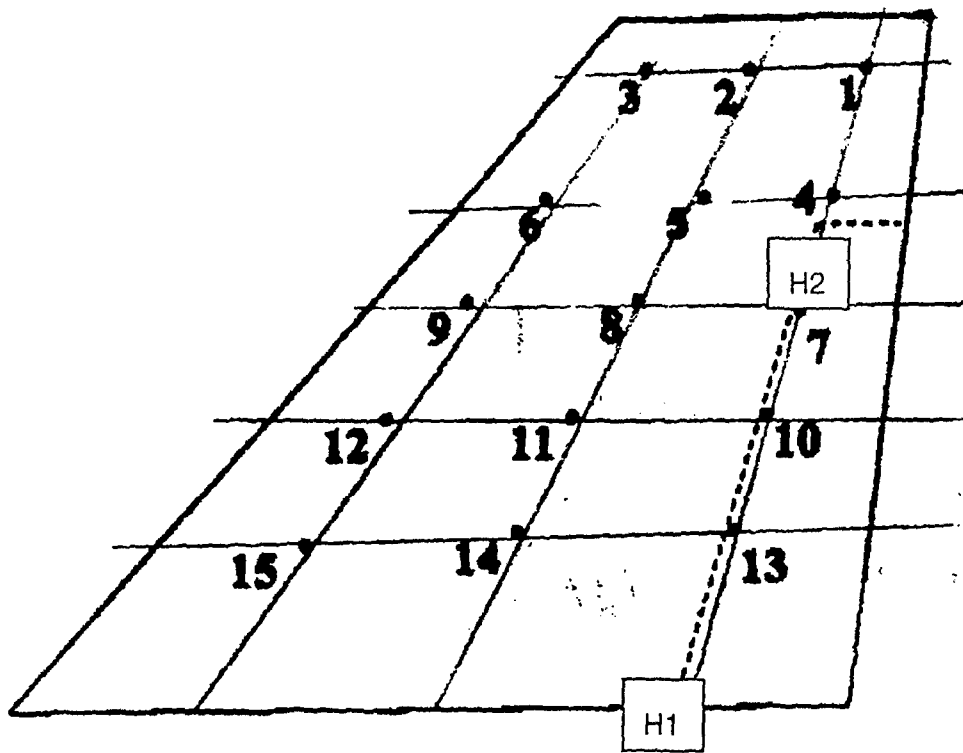
Figure 3-1. A Typical Aerodynamic Surface (e.g. a Vertical Tail)
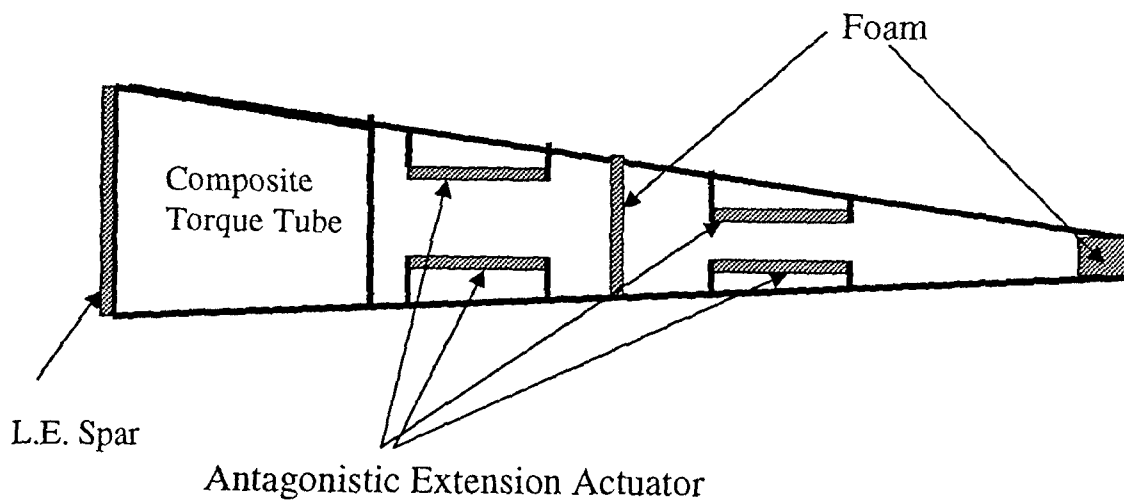
Figure 3-2. A Typical cross-section and Assembly of an Active Control Surface
(U. S. Patent Pending)

A conventional control surface, when used in conjunction with an active control system, produces a rigid body rotation about the hinge line H1-H2 at low frequencies, since these are heavy. For example, the rudder of a typical fighter aircraft weighs about 64 pounds. It is

difficult to swing this massive control surface about a hinge line in excess of 30 cycles per second (Hertz). In contrast, the present ACSM device weighs less than 5 pounds and hence it is able to deform rapidly in a complex pattern. This complex surface can be actuated at significantly high frequencies that encompass the complete spectrum of buffet loads.
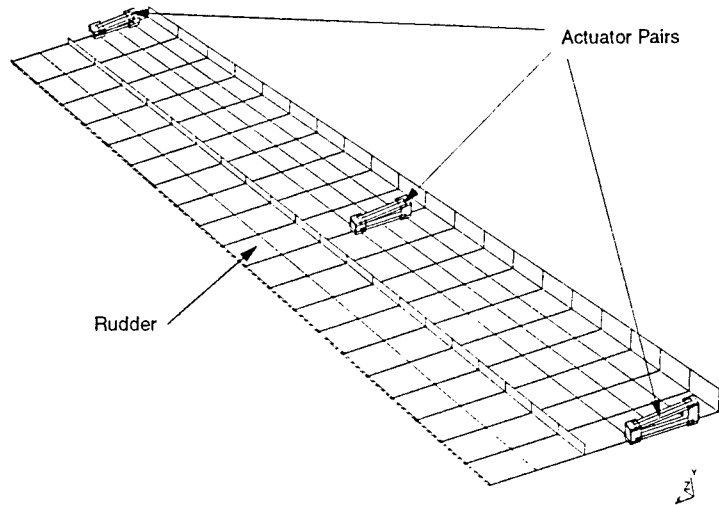
Figure 3-3. Control Surface Showing Imbedded Smart Actuators
(U. S. Patent Pending)

Control Surface Mode 1
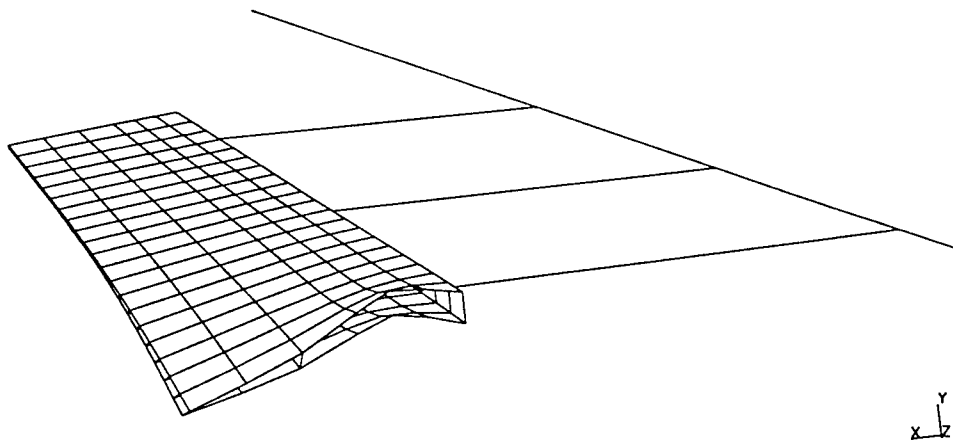
Figure 3-4. Actuator Activated Control Surface Mode No. 1
(U. S. Patent Pending)

24

Control Surface Mode 3
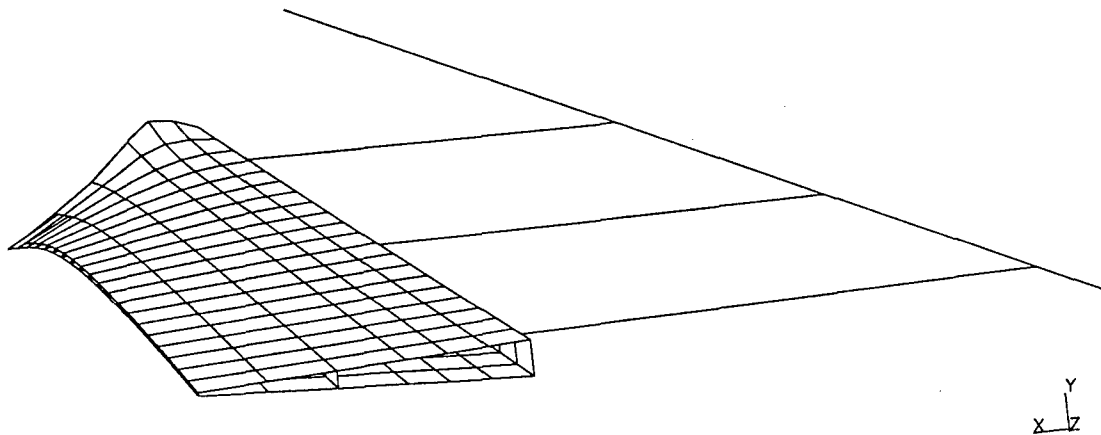
Figure 3-5. Activated Control Surface Mode No. 3
(U. S. Patent Pending)

3.2 Selection of Smart Actuators

A smart actuator is a device that exerts force to change shape or position of a component. This process involves a significant amount of force and displacement. A conventional actuator of hydraulic or pneumatic type is known to fall into this category. However, these devices are limited to a low frequency spectrum. In the rapidly advancing materials technology, new systems of actuators that operate in the high frequency range are being developed. However, these actuators are limited to small displacements. Therefore, displacement amplifications are required to enhance their performance characteristics. In the proposed study, readily available actuators were reviewed and a few suitable actuators that satisfy force, displacement, weight and packaging criteria were recommended for laboratory evaluation. Specific details of these actuators are presented next.

3.2.1 Actuator Type 1: Low Volt Lightning Bolt Extension Motor

Figure 3-6a shows a schematic outline of an inexpensive off-the-shelf delivery type actuator, which is made of two active piezoceramic plates. The key advantages of this product are:

- Speedy installation using four bolts,

- Re-use in multiple tasks,

- Solid metal internal strength reinforcement,

- An internal bleed resistor protects the actuator and the electrical circuit from the pyro-electrically-generated voltages,

- Has extremely low magnetic permeability,

25

- No significant magnetic field generation.

Some salient specifications are presented in Table 3-1.

Offered by	Piezo Systems, Inc., 186 Massachusetts Avenue, Cambridge, MA 02139
Model No.	T226-A4-503-LME, Lightning Bolt Extension Motor
Piezo Material	5A-S4-ENH
Max Displacement	7 μM (0.0003 inch)
Max operating Volt	160 V
Push/Pull	250 N (56.5. Lbs.)
Weight	14 gms (0.03 lb.)
Response time	25 micro seconds

Table 3-1 Specifications of Actuator Type 1

This actuator is specially made for structural vibration control. Each piece is available for less than $200. If these actuators prove to function satisfactory, more of these can be used in a distributed control configuration shown in Fig. 3-2.
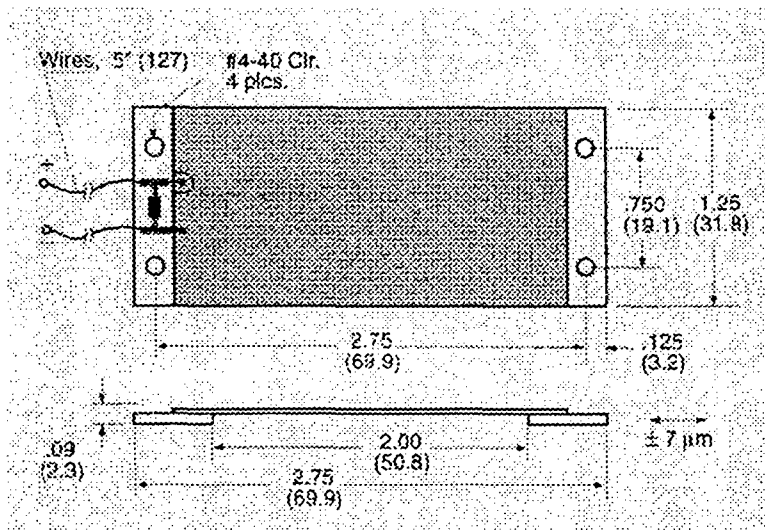
Figure 3-6a. Piezoceramic Extension Motor

3.2.2 Actuator Type 2: High Volt Piezoceramic (PZT)

These are medium priced stacked piezoceramic actuator units in the high voltage category. A typical actuator assembly, depicting the attachment of electrodes in each layer and the poling direction, is shown in Figure 3-6b. The pulling force of the Type 2 actuator is slightly higher than that of actuator Type 1. However, high volt actuators offer larger extensions. Some customized products are available at slightly higher price. Although high volt units are rated at 1000V as the operating range, the input stimuli are only 10V. A power amplifier boosts the voltage and recovers the out-of-phase component of the power. Hence, there is no need to dissipate the unused energy. Hence, the power consumption is minimal. Some salient specifications of this product are presented in Table 3-2.
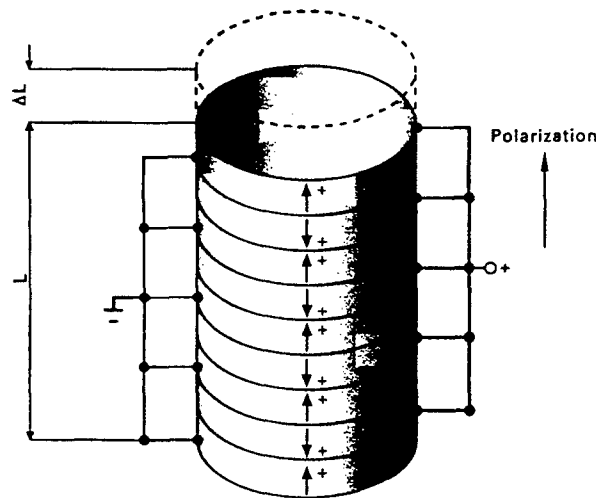
Figure 3-6b. A Typical Piezoceramic Stack Actuator (PZT)

Offered By	DynaOptic Motion Corporation, 23561 Ridge Route, Laguna Hills, CA 92653
Model No.	Pst 1000/10/125 VS18 Preloaded
Displacement range	125 μm (0.0046 inch)
Pushing force	2000 Newtons (450.0 Lbs.)
Pulling force	300 Newtons (67.5 Lbs.)
Resonance Frequency	5.0 kHz
Weight	10 oz (0.625 Lbs.)
Max Operating Volt	1000 V
Amplifier with energy recovery	AVG 430/08, amplifier

Table 3-2 Specifications of Actuator Type 2

3.2.3 Actuator Type 3: High Volt Piezoceramic (PZT)

These are preloaded load PZT actuators, and are based on highly sophisticated electronic technology. Hence, they provide high force and large displacement. Some salient specifications are presented in Table 3-3.

Offered By	Polytec PI Inc., 1342 Bell Avenue, Tustin, CA 92780
Model No.	P-246.77 Preloaded open and closed loop
Displacement range	120 µm (0.0046 inch)
Pushing force	12,500 Newtons (2,810. Lbs.)
Pulling force	2,000 Newtons (450. Lbs.)
Resonance Frequency	3.0 kHz
Weight	830gms (1.83 Lbs.)
Max Operating Volt	1000 V
Amplifier with energy recovery	E-480.00

Table 3-3 Specifications of Actuator Type 3

3.3 Modeling of Piezoelectric Actuators

A PZT actuator can be represented by a mechanical spring and mass system, which is depicted by an equivalent circuit diagram shown in Figure 3-7. In slow movements, the Capacitance C_0 is apparent, while at higher frequencies the resonance characteristic of parallel connection plays an important role. The resonance frequencies of the PZT actuators are in kHz. These can function as actuators up to 60% of their resonance frequencies. Thus, PZT actuators can provide sufficient excitation to generate aerodynamic damping over the entire spectrum of buffet loads.
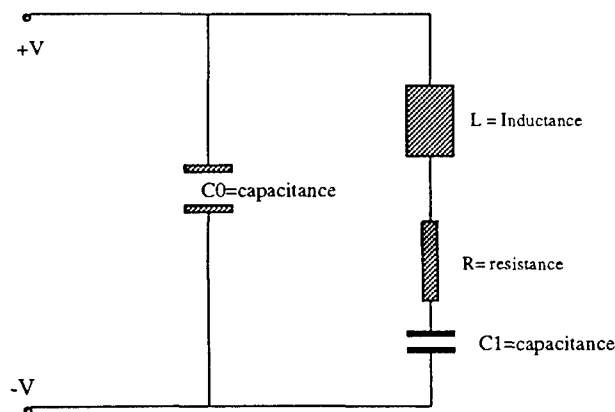
Figure 3-7. Mathematical Representation of the PZT Actuator

These PZT actuators are manufactured by the Physic Instrument Company and are made available with built-in closed-loop units as shown in Figure 3-8. The input volt varies from zero to 10 volts, which is proportional to the acceleration signal, g.
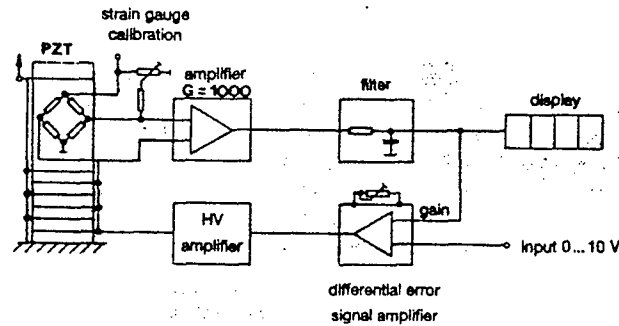
Figure 3-8. Closed Loop Control Diagram with Actuator Displacement Sensor

Figure 3-9 shows a schematic outline of the active control system in which the output, u, of the controller, K, becomes the input to the PZT controller (Figure 3-8). Thus, Figure 3-9 depicts a typical layout of the plant and the inter-connection of external input (buffet or gust), acceleration sensors, active controllers, actuator controllers (PZT power amplifier) and actuators. This ACSM device, along with an independent computerized active control system, can be used to suppress flutter, buffet and gust loads with greater reliability and without interfering with the primary flight control system. A brief description of theory that inter-connects all these disciplines is presented next. More specific details of theory and implementation are available in the U.S. Air Force Reports, References 14 and 15.
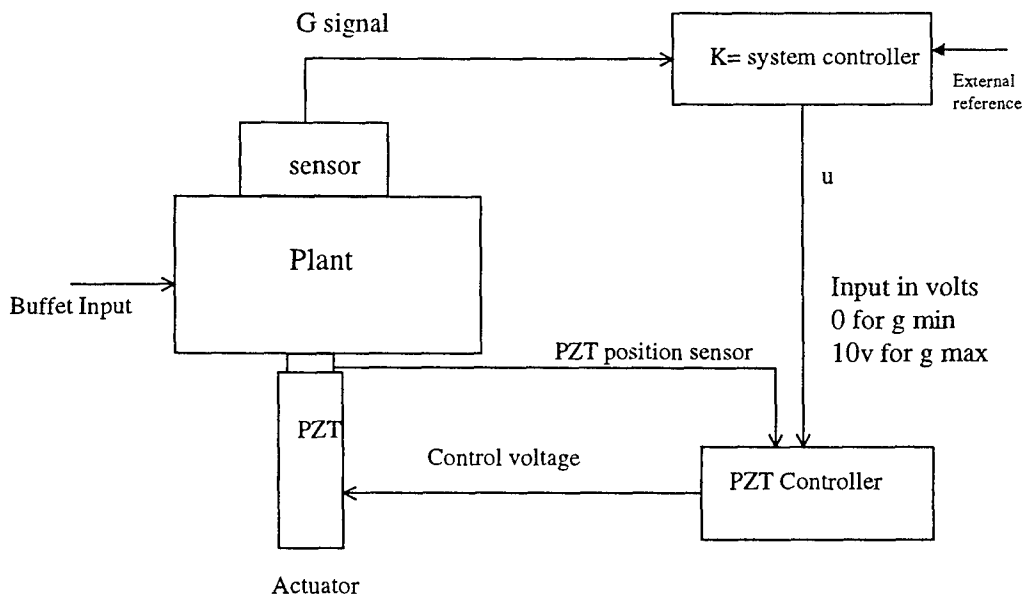
Figure 3-9.Assembly of Sensor, Controller and Actuators

3.3.1 Controller Design

Let us now consider the theoretical aspects of the active controller design. The equations of motion in the state space coordinate system can be written as:

$$\dot{X} = AX + B_{ext}f_{ext} + B_u u \tag{3-1}$$

where:

X = State space vector comprising of displacements and velocities

A = Generally called a plant matrix comprising of structural stiffness, inertia and unsteady aerodynamic matrices

B_{ext} = Matrix related to buffet or gust load vector, f_{ext}

B_u = Active control surface modal (ACSM) matrix that relates to the actuator electrical stimuli, u, in volts

The output quantities (stress and accelerations) are given by:

$$Y = \begin{Bmatrix} \sigma \\ g \end{Bmatrix} = \begin{bmatrix} C_1 & D_{11} & D_{12} \\ C_2 & D_{21} & D_{22} \end{bmatrix} \begin{Bmatrix} X \\ f_{ext} \\ u \end{Bmatrix} \tag{3-2}$$

Where:

σ = A stress vector

g = An acceleration vector

f_{ext} = Buffet or gust load vector, either in frequency or time domain

u = Actuator input stimuli in volts or amps depending on the type of actuators used

The MATLAB analysis tool was used to compute the control gain matrix K such that the actuator stimuli is related to the sensor output, acceleration g:

$$u = Kg \tag{3-3}$$

Then, eliminating u in equations (3-1) and (3-2), the closed loop system in the frequency domain can be written as:

$$\sigma(\omega) = G(\omega)f_{ext}(\omega) \tag{3-4}$$

The corresponding stress power spectral density can be computed from equation (3-4).

Figure 3-10 shows the general layout of the active control algorithm that connects the external buffet load to the stress output as defined by equation (3-4). Computer software of the active control algorithm can be written and implemented into an aircraft. Thus, a single device can be

used to reduce buffet and gust loads and to eliminate flutter within the flight envelope of the aircraft. Typical examples that demonstrate the proof of concept are presented in the next Section.

$\sigma = stress$

SYS =(A,B,C,D), PLANT

Buffet load

G= acceleration

$\upsilon = Actuator\ stimuli$

K = Controller
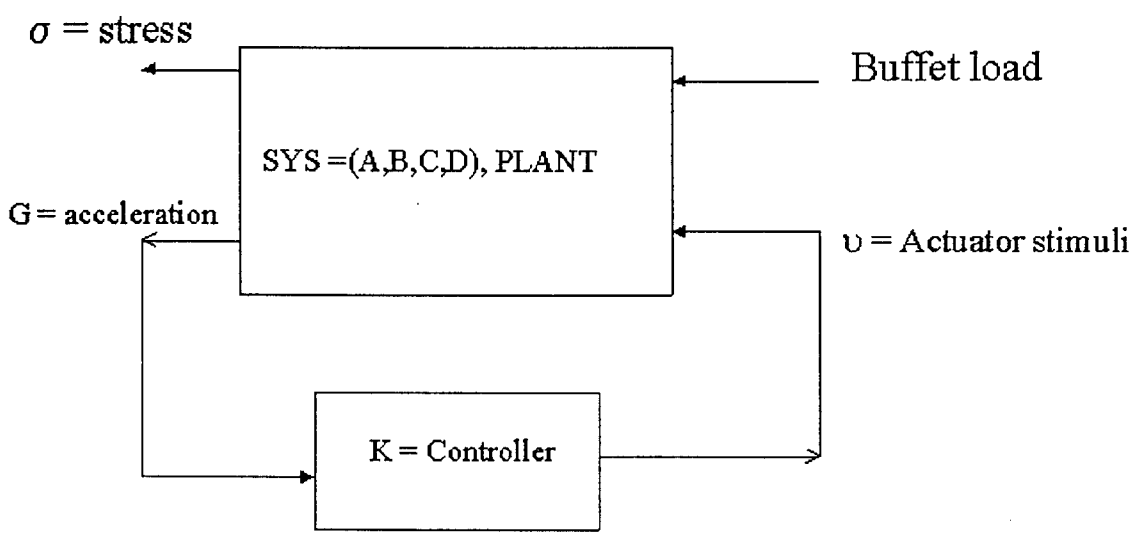
Figure 3-10. Closed Loop Control System

31

4 DISCUSSION OF RESULTS

To demonstrate the proof of concept of the active control surface modal device, the F-18 twin-tail military aircraft was selected to conduct buffet and gust response analyses. Specific details of the analyses are presented in the following sections.

4.1 Data Files From ASTROS

A number of MAPOL routines were developed in ASTROS (Ref. 16) to compute necessary data files such as generalized stiffness, mass, unsteady aerodynamic coefficient matrices, control surface modes, acceleration sensor and stress output matrices. These data files were used to develop a load alleviation module in the MATLAB platform (Ref. 17).

4.1.1 Generalized Coordinate Matrix

The control surface modes that deform the rudder under the influence of unit forces applied at the actuator attachment points were computed in ASTROS. Next, ten vibration modes of the vertical tail were computed. Three high frequency modes were replaced by the control surface modes. Then, the so-called modal approach was used to compute the necessary generalized matrices and forces in the usual sense. The ACSM approach provides more effective aerodynamic controllability than that of rigid body rotation of the control surface. In other words, this device has the ability to create large aerodynamic damping in precise out-of-phase mode and at high frequencies when needed.

4.1.2 Acceleration output matrix

Two acceleration sensor points, one at the leading edge and other at the trailing edge of the vertical tail tip section were selected. A transformation matrix, C, that relates to the generalized coordinates to the acceleration sensors was computed as:

$$g = C * \dot{X} \qquad (4\text{-}1)$$

where X is the state vector and g is the acceleration vector in units of g. A control law will be derived that uses g as the sensor to drive the actuator voltage controller. Thus, an appropriate phase relation between the rudder motion and vibration of the vertical tail will be established to minimize the buffet induced dynamic response.

4.1.3 Stress output matrix :

A similar transformation matrix that relates the root stress to the state space vector was computed. This relation is given by:

$$\sigma = S * X \qquad (4\text{-}2)$$

where S is the stress relational matrix and σ is the stress in psi at the root section.

4.2 Dynamic Load Alleviation Code Development in MATLAB

MATLAB and Mu Analysis Tools (Refs. 17 and 18) were selected as the basic platforms to develop the buffet load alleviation system. These tools provide a number of built-in matrix operation commands, eigenvalue routines, and open and closed loop response analysis capabilities. In addition, a few m-file routines were developed and included in the analysis system. The following are the additional m-files developed:

(a) Smart Actuator model to compute the actuator force matrix F_u.

(b) Pade approximation module to transform the frequency based Qhh data in terms of state matrices, such as:

$$Qhh(k) = A_1 + ikA_2 - (ik)^2 A_3 + (\frac{ik}{\beta + ik})A_4 + \ldots\ldots$$

(c) Buffet load module to compute the generalized buffet load using measured power spectral density data.

(d) Gust velocity module to express the frequency domain based Dryden and Von Karman gust spectra. The code was developed in a general form such that the buffet spectra can also be expressed in terms of discrete time pressure data. Thus, the gust and buffet response analysis and load alleviation analysis can be performed in a similar manner.

(e) Plant Matrices module. This module sets up the state space matrices A , B and f such that:

The State Space Equation is given by:

$$\dot{X} = AX + B_1 u + B_2 f$$

The Output Matrix consisting of stress and accelerations is given by:

$$y = CX + D_1 u + D_2 f$$

Then, the System Matrix:

$$\text{Sysm} = [A, B_1 B_2 C, D_1 D_2]$$

was formulated in MATLAB.

Here, u is the actuator input, and f is the external disturbance forces such as gust and buffet loads.

(f) A flutter solution module was developed to compute the roots of the plant matrix, A, for a given list of air densities and velocities.

33

4.3 Vibration and Flutter Analysis

The stiffness and mass properties of the F18 vertical tail was represented by means of beam elements. However, a new rudder that incorporates three pairs of smart actuators was designed to represent the vibration characteristics of the original tail configuration.

Figure 4-1 shows an overview of the finite element model of the vertical tail and the rudder, while Figure 3-3 shows the finite element model of the rudder and the location of three actuators. Figures 4-2a through 4-2c show the actuators generated rudder deformation modes. Figures 4-3 through 4-7 show the first five vibration mode shapes of the vertical tail and rudder assembly. The vibration modes and the rudder control surface modes were adjoined to form a generalized system of modes to compute the generalized stiffness, mass and aerodynamic forces. Here, the rudder modes are not orthogonal to the vibration modes, and are not required to be.
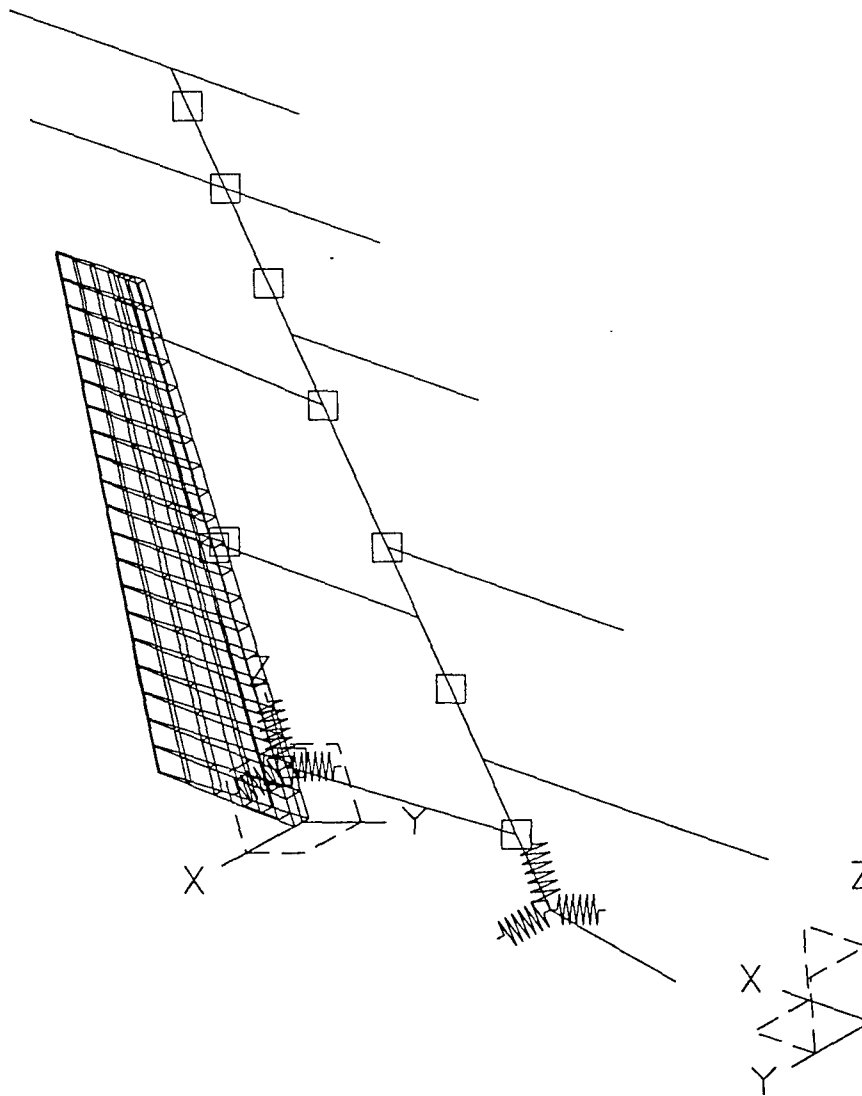
Figure 4-1. Finite Element Model of Vertical Tail of a Twin Fin Military Aircraft

Figures 4-8 through 4-11 show the correlation of Pade fit for real and imaginary data of the frequency dependent Qhh. One aerodynamic lag term was used in this analysis. Correlations are seen to be very good. However, an option exists to include additional lag terms if necessary.

Control Surface Mode 1
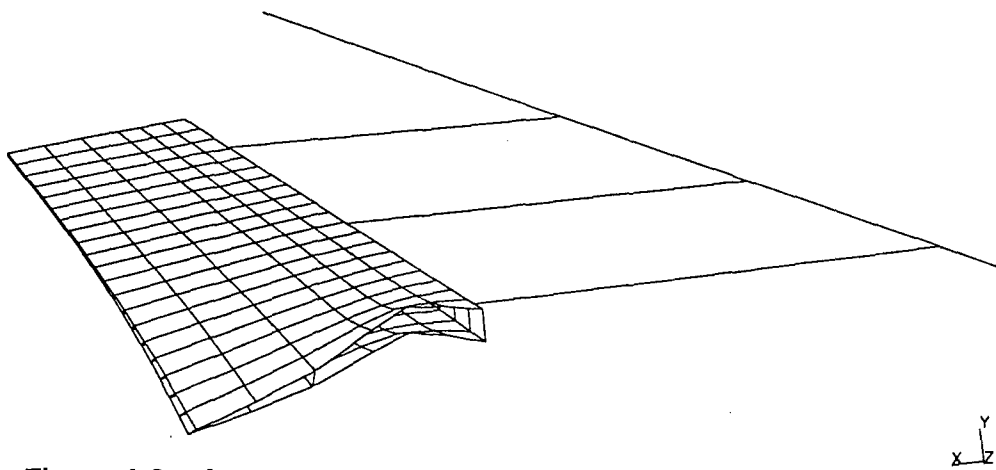
Figure 4-2a. Actuator Imposed Rudder Modes (U. S. Patent Pending)

Control Surface Mode 2
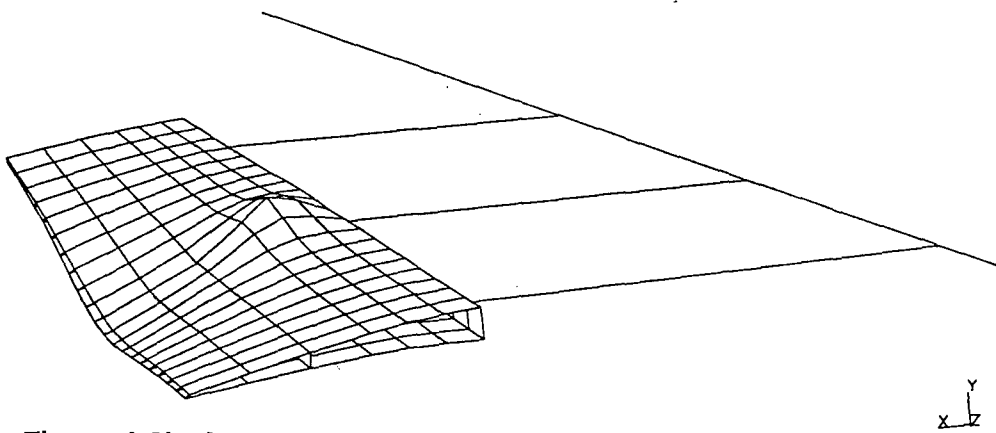
Figure 4-2b. Actuator Imposed Rudder Modes (U. S. Patent Pending)

Control Surface Mode 3
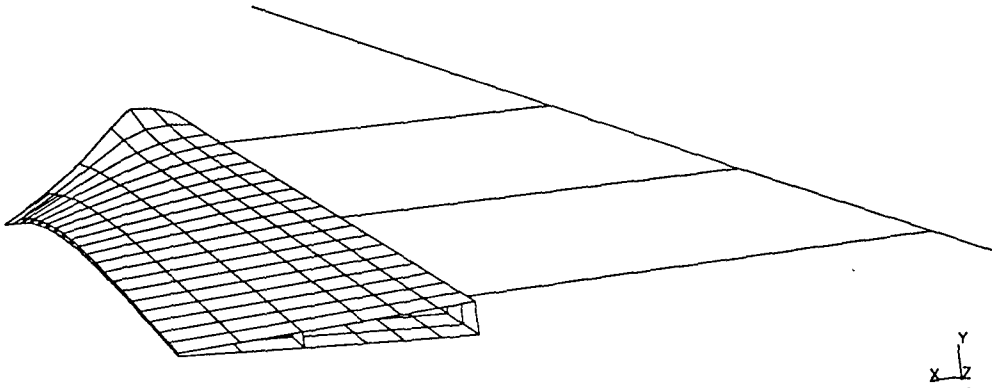
Figure 4-2c. Actuator Imposed Rudder Modes (U. S. Patent Pending)

DEFORMATION: 1-B.C. 0,MODE 1, DISPLACEMENT-1   ASTROS Results - Elastic Mode 1
MODE: 1   FREQ: 16.387
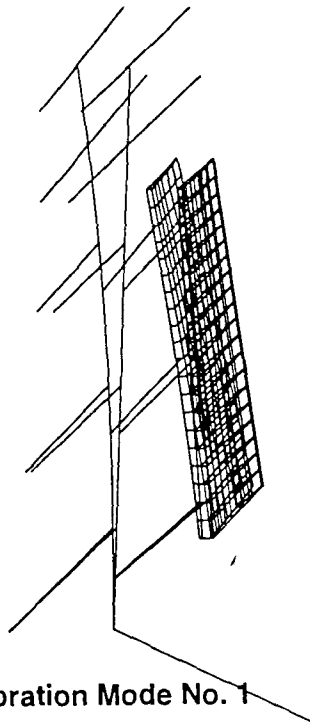
Figure 4-3 Vibration Mode No. 1

DEFORMATION: 2-B.C. 0,MODE 2, DISPLACEMENT-2   ASTROS Results – Elastic Mode 2
MODE: 2   FREQ: 35.646
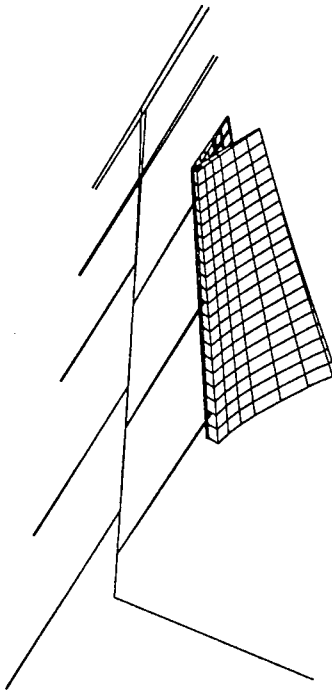
Figure 4-4 Vibration Mode 2

DEFORMATION: 3-B.C. 0,MODE 3, DISPLACEMENT-3   ASTROS Results – Elastic Mode 3
MODE: 3   FREQ: 47.856
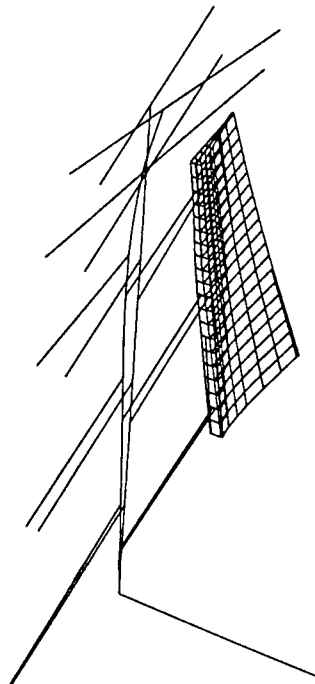
Figure 4-5 Vibration Mode 3

37

DEFORMATION: 4-B.C. O.MODE 4, DISPLACEMENT-4   ASTROS Results - Elastic Mode 4
MODE: 4   FREQ: 63.182
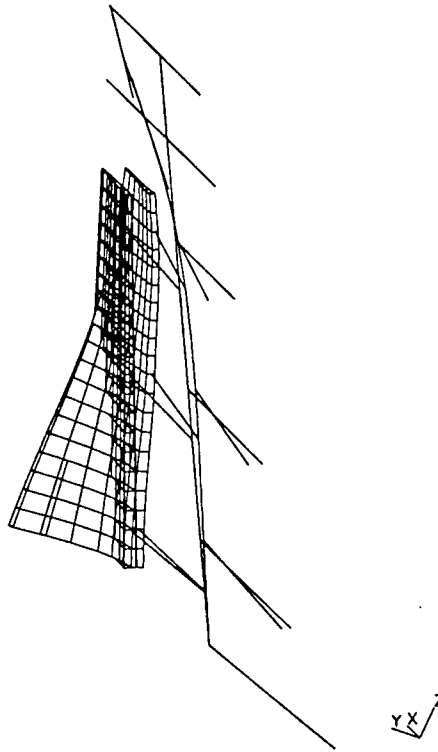
Figure 4-6 Vibration Mode 4

DEFORMATION: 5-B.C. O.MODE 5, DISPLACEMENT-5   ASTROS Results - Elastic Mode 5
MODE: 5   FREQ: 80.527
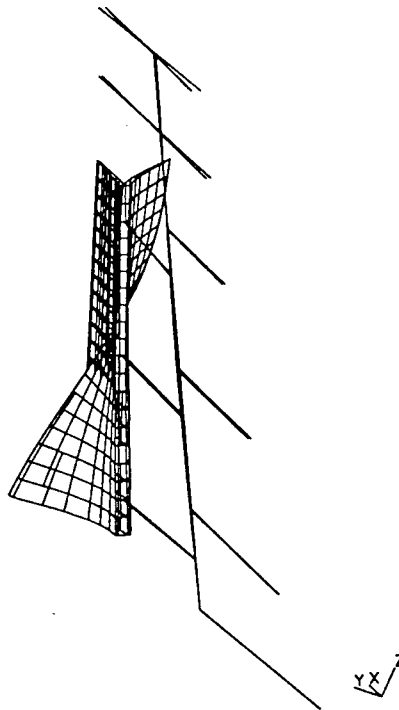
Figure 4-7 Vibration Mode 5

38

Correlation of Pade fit - vs Original data +
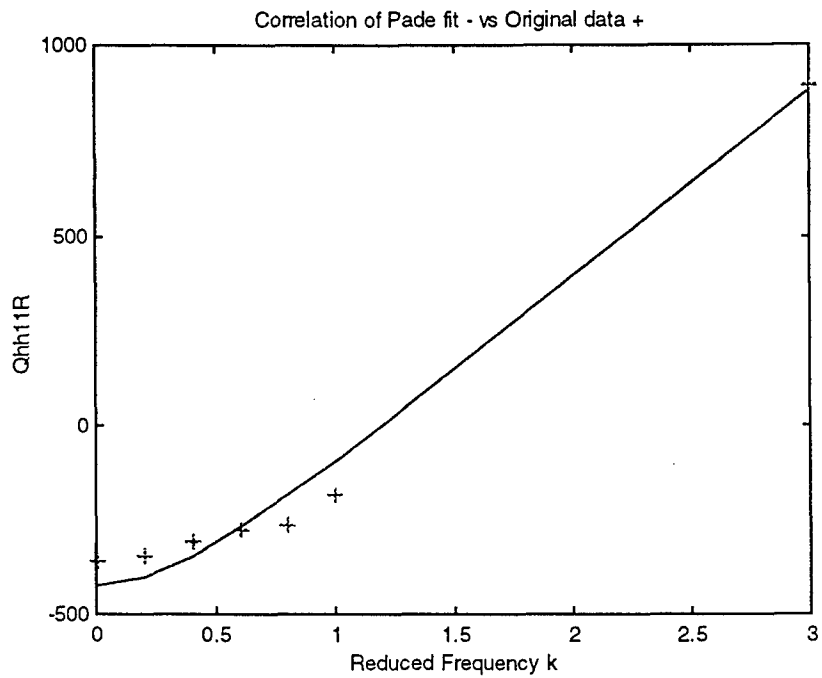
Figure 4-8 Correlation of Pade Approximation to Q11-real

Correlation of Pade fit - vs Original data +
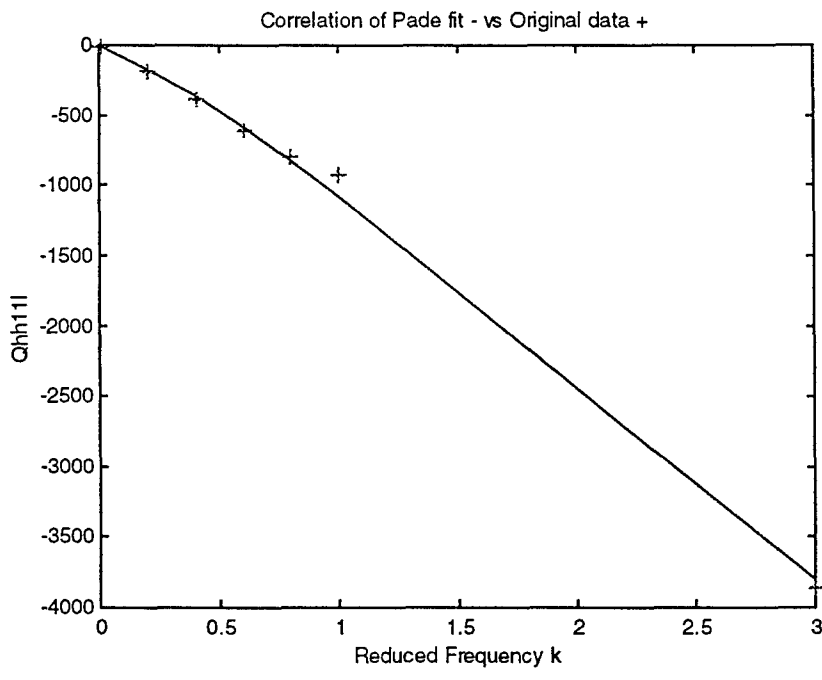
Figure 4-9. Correlation of Pade Approximation to Q11-imag

39
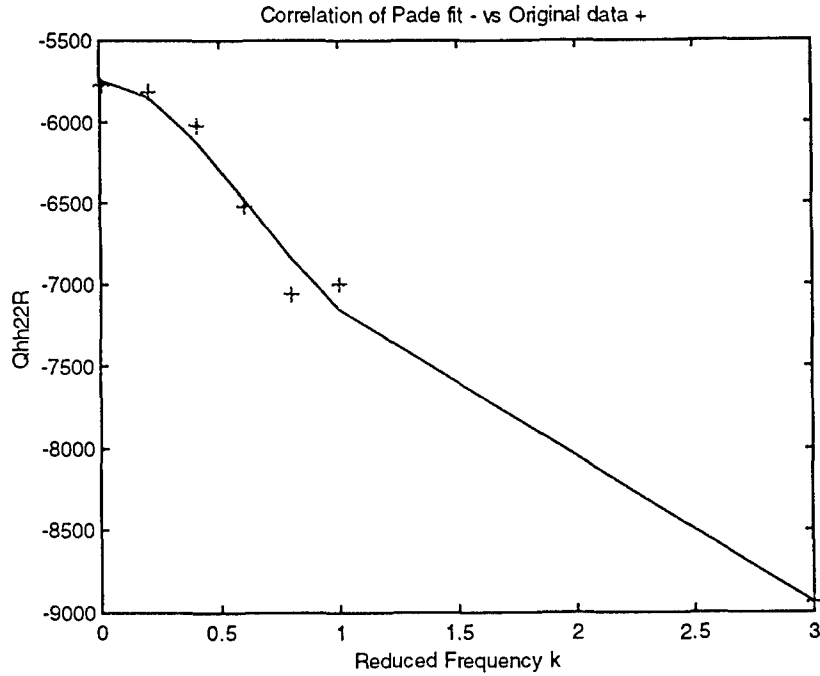
Figure 4-10 Correlation of Pade Approximation to Q22-real
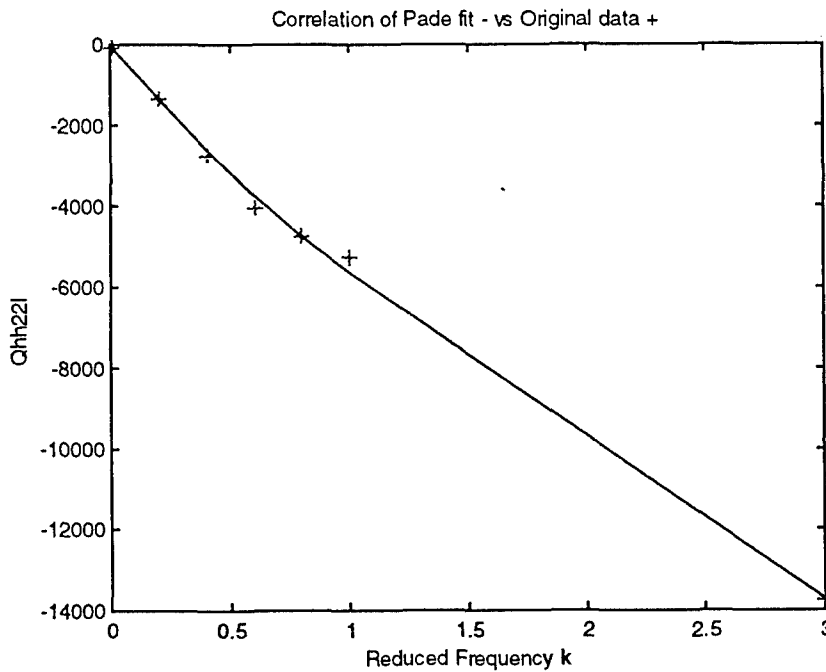
Figure 4-11 Correlation of Pade Approximation to Q22-imag

Using the state space formulation, the flutter solutions were conducted to assure the redesigned model is free of flutter instabilities. Figures 4-12 through 4-15 show the results of the flutter solution for M=0.8 at sea level. The variation of frequencies vs. dynamic pressure for

modes 1 through 5 are shown in Figures 4-12 and 4-13, while the plots of aerodynamic damping for the corresponding modes are presented in Figures 4-14 and 4-15. The vertical tail was found to be flutter free at this Mach number and the dynamic pressures used.

Frequency in mode 1 and 2
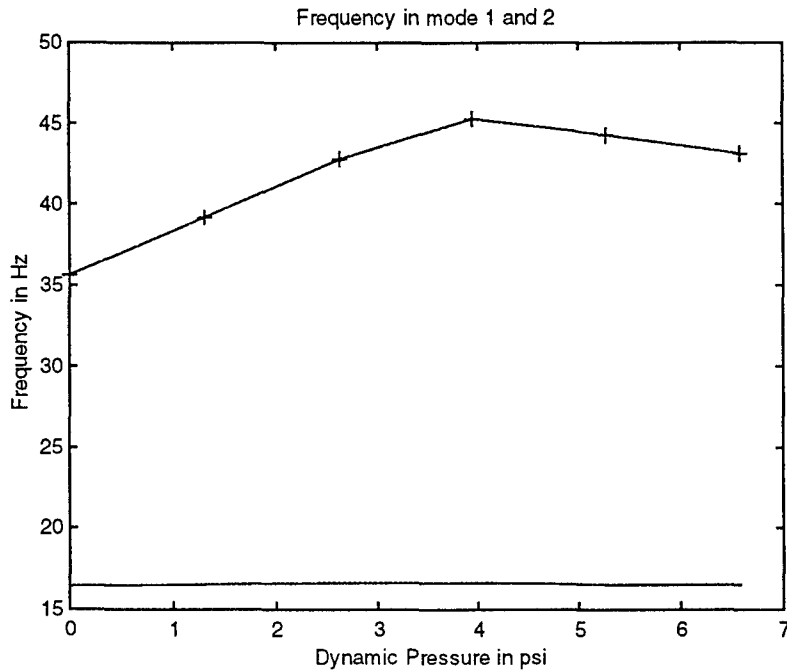
Figure 4-12. Frequencies in Modes 1 and 2 vs. Dynamic Pressure

Freq in mode 3, 4 and 5
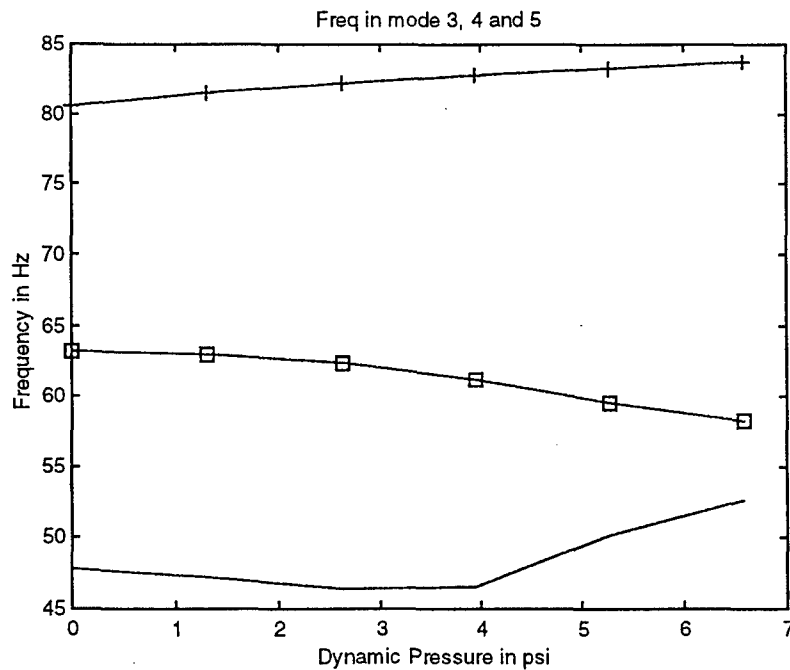
Figure 4-13. Frequencies in Modes 3, 4 and 5 vs. Dynamic Pressure

41
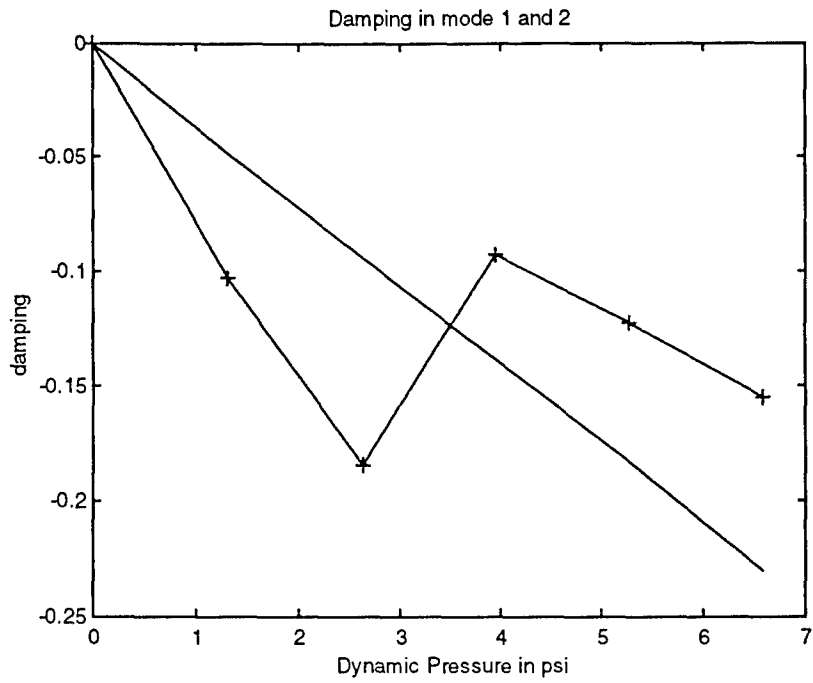
Figure 4-14. Damping in Modes 1 and 2 vs. Dynamic Pressure
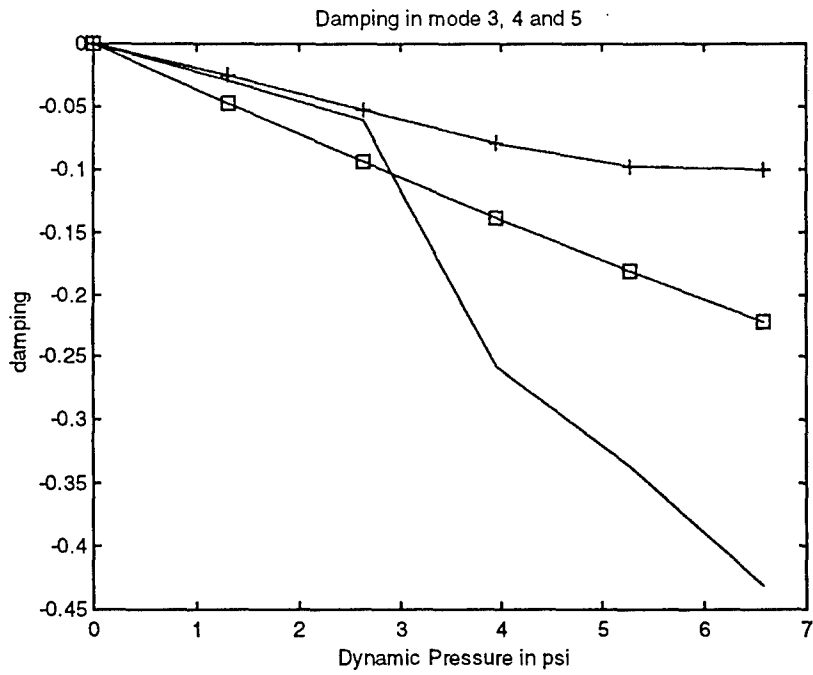
Figure 4-15. Damping in Modes 3, 4 and 5 vs. Dynamic Pressure

42

4.4 Gust Response Analysis

A gust response analysis was performed using the Dryden gust spectra with a RMS value, w = 50 ft/sec and flight speed, V_0 = 893 ft/sec at sea level. Figure 4-16 shows the Dryden power spectral density (PSD) of gust in terms of angle of incidence, i.e. $\alpha_g = \dfrac{w}{V_0}$, where w is the vertical gust velocity and V_0 is the flight velocity. This PSD was transformed into the discrete time data such as gust angle of incidence vs. time. Figure 4-17 shows a typical generalized gust load in vibration mode 1. The corresponding transient load is presented in Figure 4-18. First an open loop gust transient response analysis was performed. Figure 4-19 shows the PSD of the tail root stress. As expected, peaks are shown at the first two fundamental modes, such as the bending and torsion.

The leading edge acceleration PSD is shown in Figure 4-20. Peaks appear at all five vibration modes. However, a significantly sharp 10g response appears at the third mode, the tail torsion. Similar data for the trailing edge acceleration are presented in Figure 4-21. The trailing edge section appears to respond more readily to 1st, 2nd, and 4th modes.
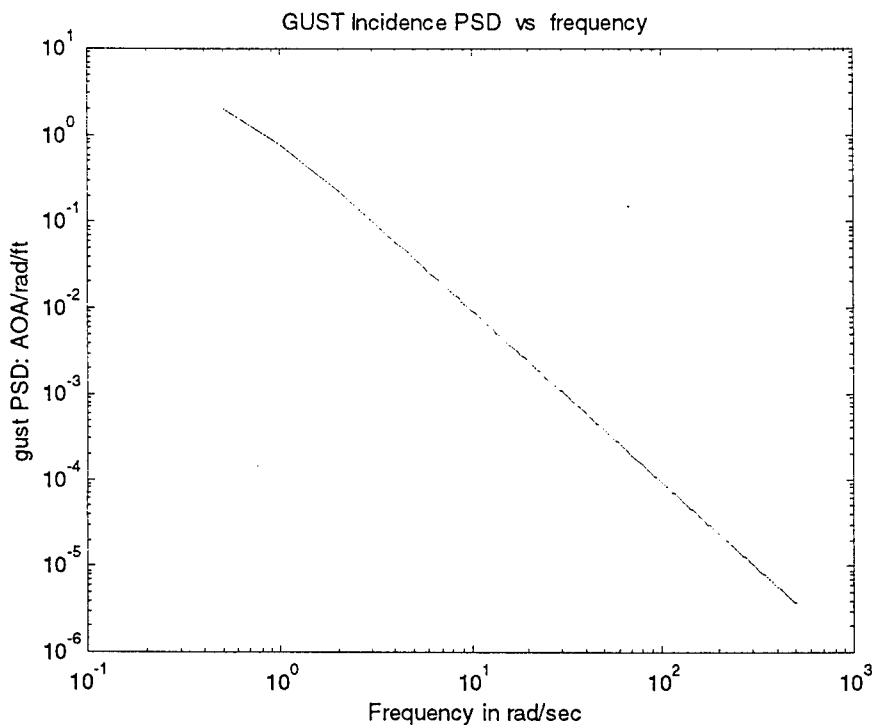

Figure 4-16. Gust Power Spectral Density,
$(w/V)^2(L/\pi)$, **vs. Frequency in Radians per Second**

PSD of GENERALIZED GUST Load in Mode 1 vs frequency
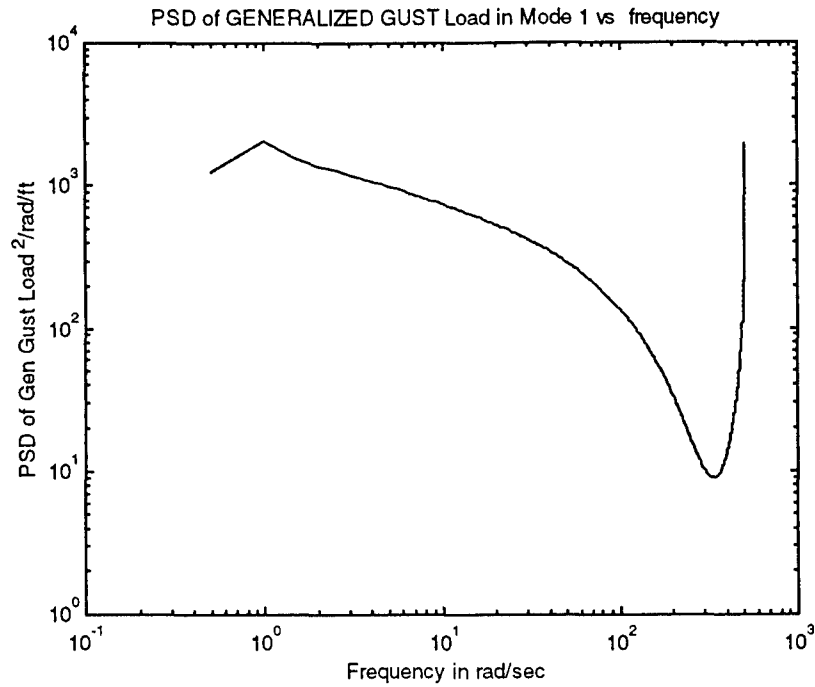
Figure 4-17. Mode 1 Gust Power Spectral Density, vs. Frequency in Radians per Second
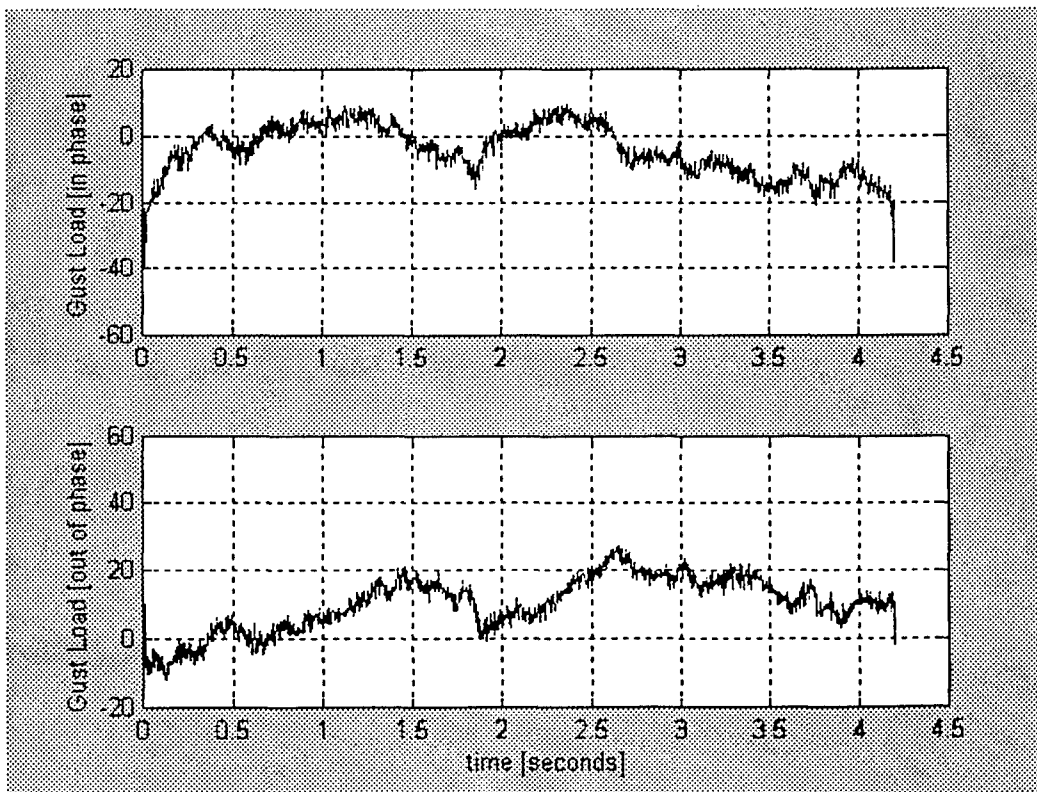

Figure 4-18. Transient Gust Load Representation in Mode 1

44
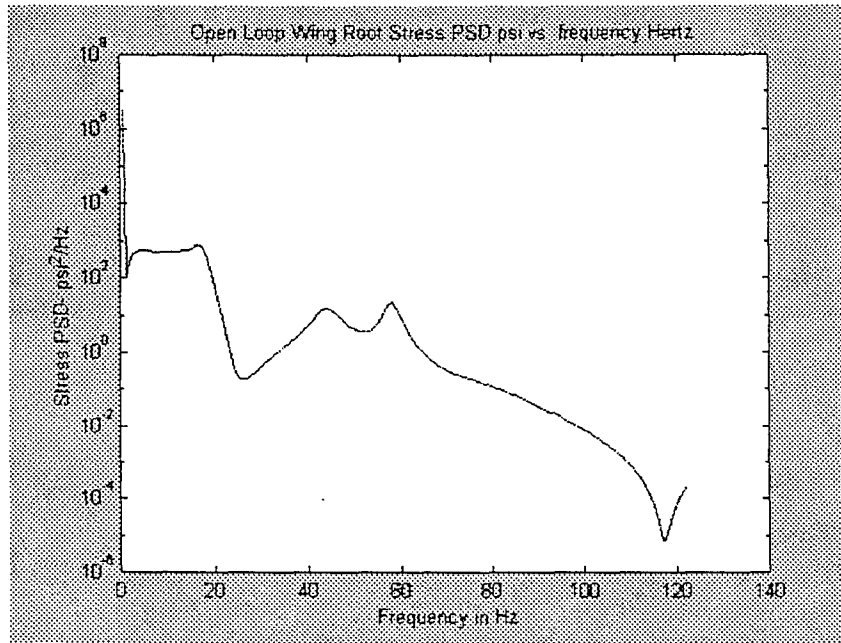
Figure 4-19. Open Loop Root Stress Spectra in Gust Analysis With RMS Stress = 1000 psi
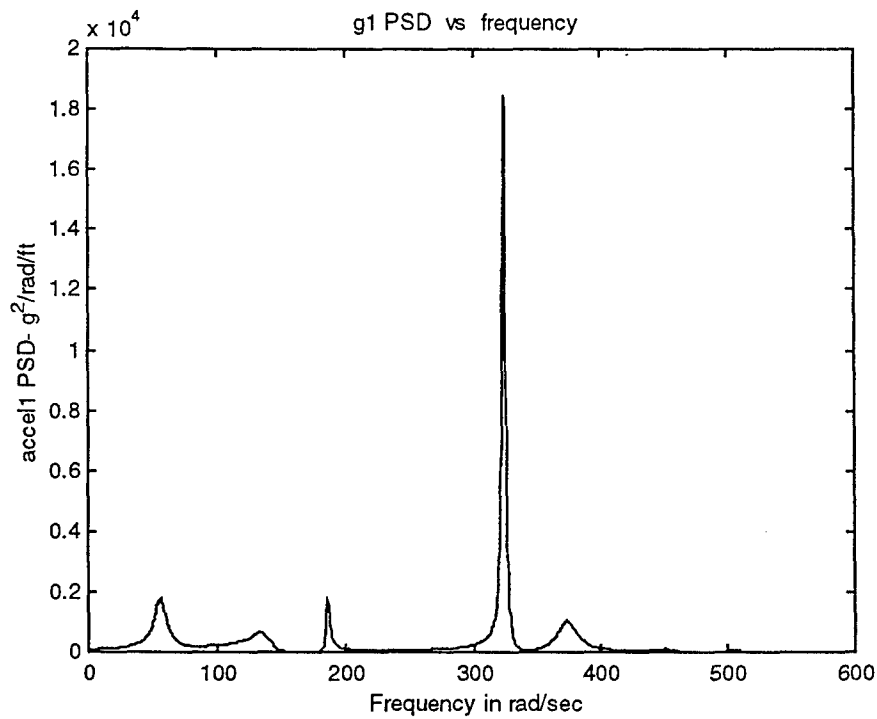
**Figure 4-20.Power Spectral Density of Wing Tip Leading Edge Acceleration vs. Frequency in rad/sec**
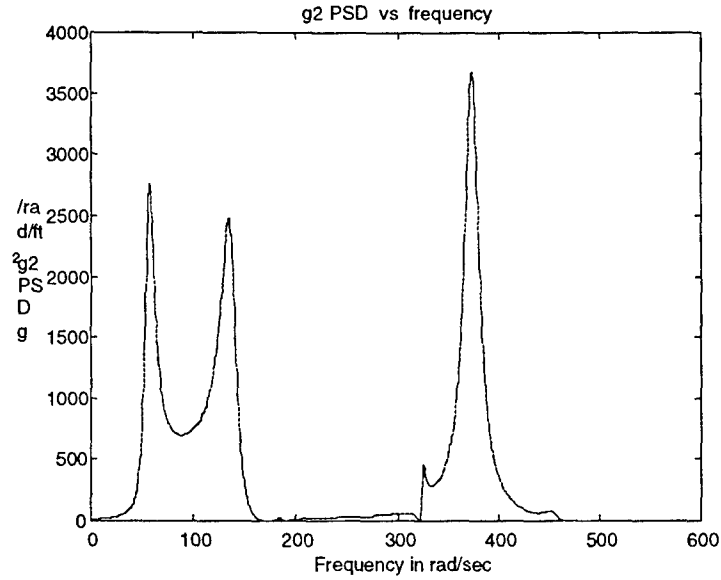
Figure 4-21. Power Spectral Density of Wing Tip Trailing Edge Acceleration vs. Frequency in rad/sec

Next, a closed loop analysis was performed using tip section accelerations as the input sensor signals. Figure 4-22 shows the PSD of the root stress distribution for the closed loop case. Although the magnitude of the stress at the time of the gust encounter is almost of same order of magnitude for both cases, the open loop RMS stress was 1000 psi verses 314 psi for the closed loop case. Thus, the active control surface modal actuation system plays a significant role in reducing the stress levels and thereby improving the fatigue life.
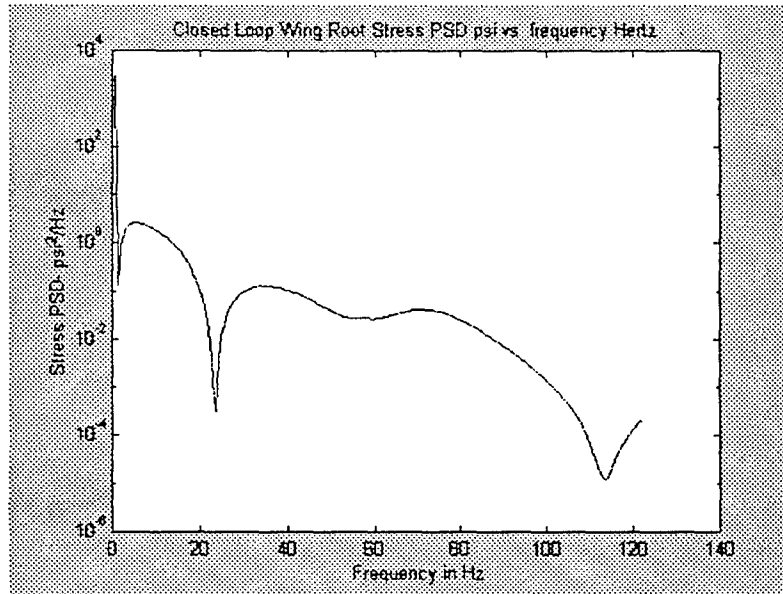

Figure 4-22. Closed Loop Root Stress Spectra In Gust Analysis With RMS Stress = 314.5 psi

4.5   Buffet Load Alleviation

NASA Langley conducted extensive buffet load measurements on a 16% scale F/A-18 model (Ref. 7). On request, NASA provided the pressure PSD data for one configuration: angle-of-attack of AOA = 34 degrees, and dynamic pressure q = 14 pounds-per-square-feet (psf). This data was first nondimensionalized in the form of power coefficient Cp vs. reduced frequency k, as shown in Figure 4-23 for all 15 data points shown in Figure 3-1. This nondimensionalized Cp vs. k data can now be applied to a full-scale aircraft. The frequency response analyses were performed using the buffet power spectral density data. The Fourier spectra were transformed into the time domain data using the inverse Fast Fourier Transform IFFT algorithm. Subsequently, the 15 point data was surface fitted over the entire tail surface and generalized forces were computed in the frequency domain.

A number of frequency response analyses were then performed for the open loop (without using the ACSM device) and the closed loop (using the ACSM device) cases. In the closed loop case, two acceleration signals measured at the wing tip were used as the feedback signals to command the actuators to minimize the root stress. The principle of dynamic load alleviation is based on generating aerodynamic damping using the active control surface modes. To demonstrate the merits of the unsteady aerodynamic damping on stress levels, three sets of analyses were conducted for two altitudes, 30,000 ft and sea level.
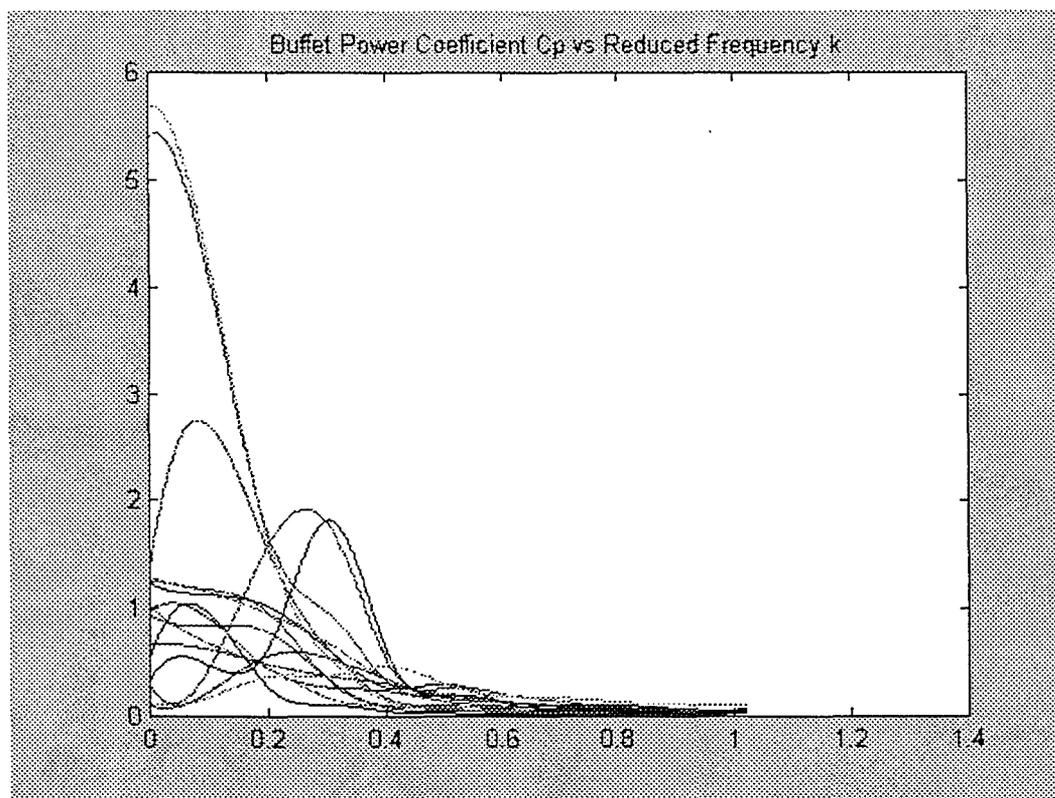

**Figure 4-23. Pressure Power Coefficient Cp vs. Reduced Frequency k
At 15 Data Points on the Vertical Tail**

These cases include:

1. Open loop frequency response analysis due to buffet loads without considering the unsteady aerodynamic forces. This is the case of a vacuum condition.

2. Open loop frequency response analysis including unsteady aerodynamic forces.

3. Closed loop frequency response analysis including unsteady aerodynamic forces.

4.5.1 Open Loop Analysis

The PSD plots of accelerations and stresses due to buffet loads for the symmetric flight condition at 30,000 ft, without unsteady air loads, are presented in Figures 4-24, 4-25 and 4-26. The peak and rms values of the corresponding data are also shown in the plots. Similar solutions that include unsteady air loads are presented in Figures 4-27, 4-28 and 4-29. Comparing these data, we note that the peak stress reduced from 570,530 psi to 15,965 psi, while the rms values reduced from 79,157.0 psi to 16,434.0 psi. Similarly, the peak acceleration reduced from 969g to 124g. This demonstrates the importance of the aerodynamic damping in dynamic load reduction methodology. Hence, the proposed active control surface modal (**ACSM**) device is expected to generate necessary damping and alleviate the dynamic effects.
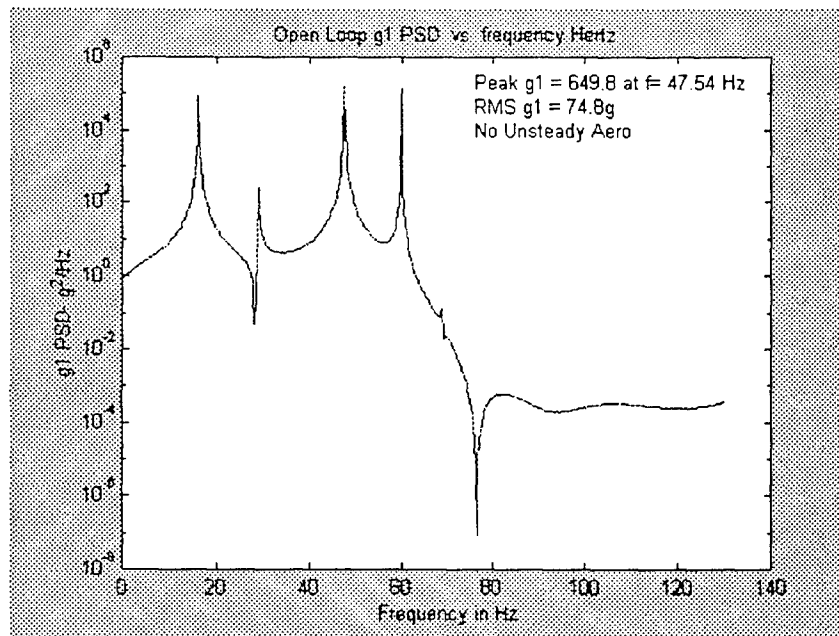
**Figure 4-24. Leading Edge Acceleration g1 PSD
Due to Buffet Load without using Unsteady Air Loads.**
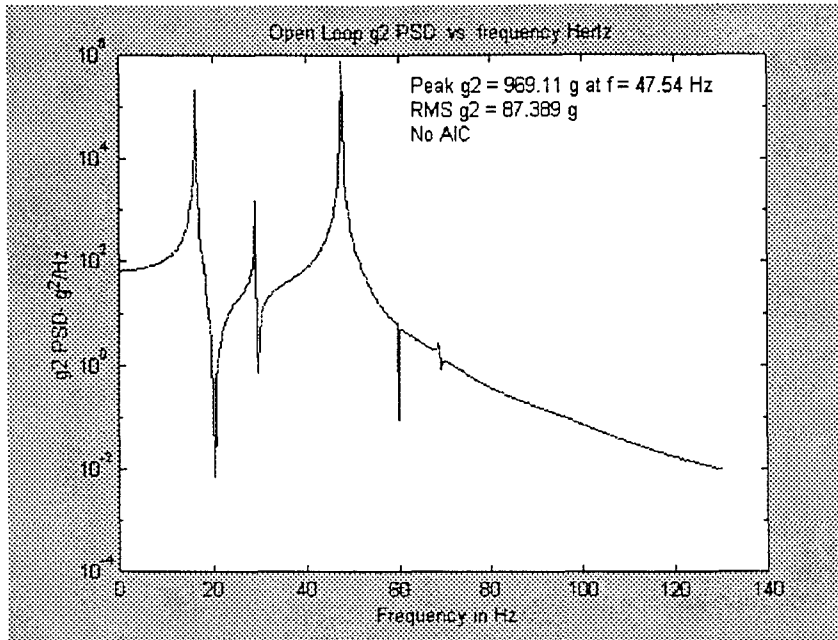
**Figure 4-25. Trailing Edge Acceleration g2 PSD
Due to Buffet Load without using Unsteady Air Loads.**
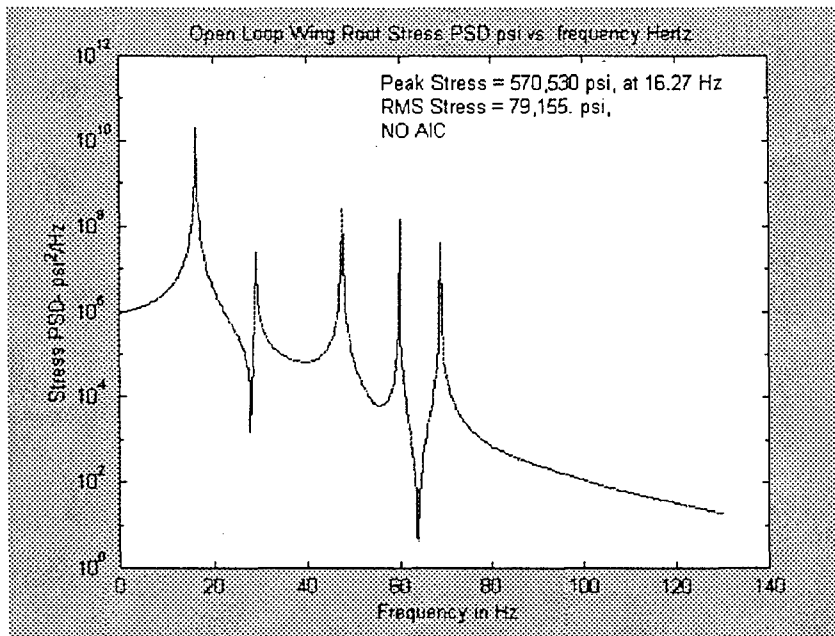
**Figure 4-26. Root Stress PSD Due to Buffet Load Without Using
Unsteady Air Loads. RMS Stress = 79,157 psi at 30k**

49
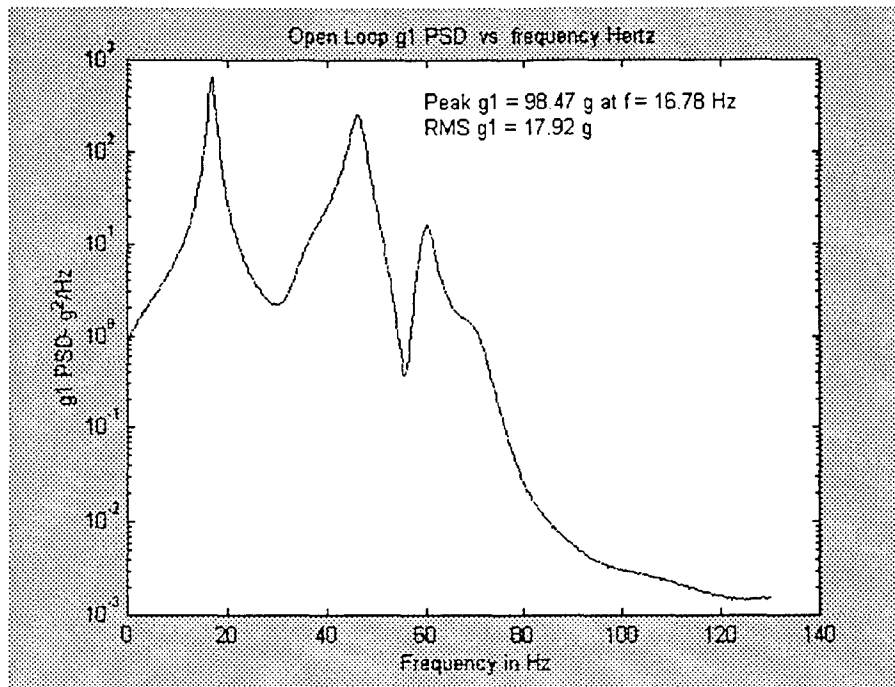
Figure 4-27. Open Loop Leading Edge Acceleration at 30k Altitude with Unsteady Air Loads
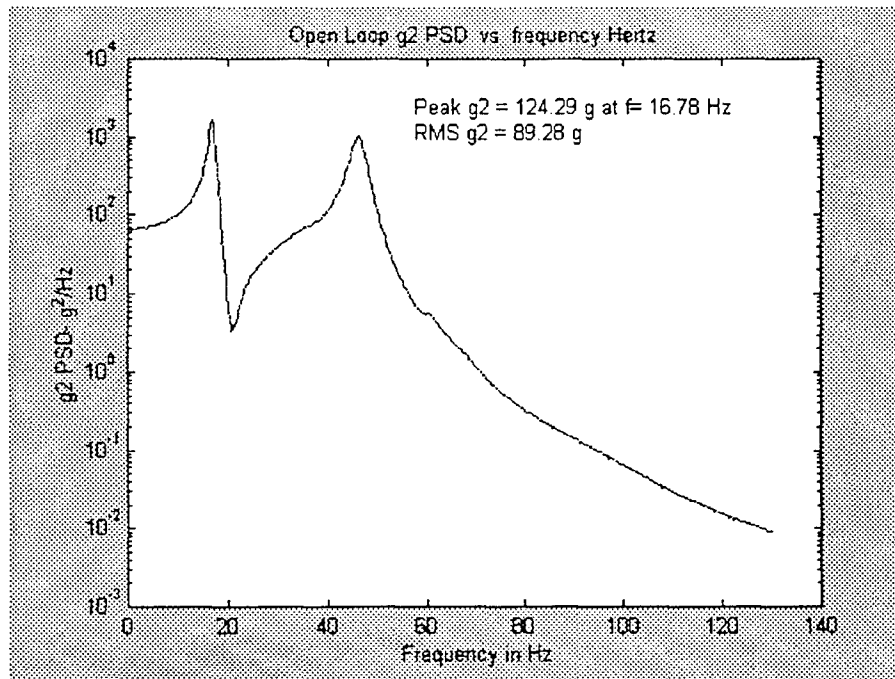

**Figure 4-28. Open Loop Trailing Edge Acceleration at 30k Altitude with Unsteady Air Loads**
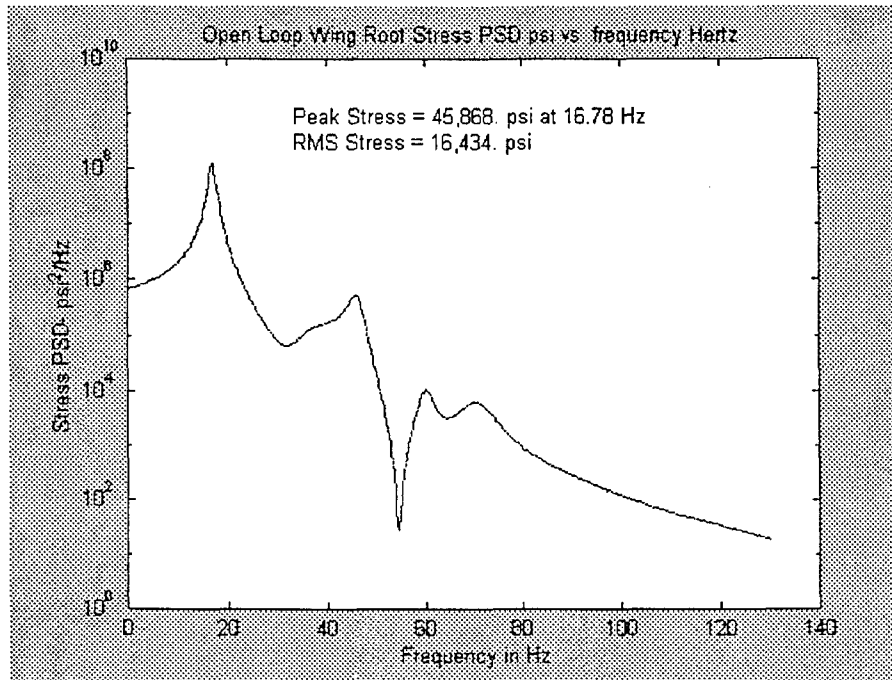
Figure 4-29. Open Loop Root Stress PSD Due to Buffet Load using Unsteady Air Load. RMS Stress = 16,434.0 psi. At 30k

4.5.2 Closed Loop Analysis at 30,000 ft Flight Condition

In this set of analyses, two acceleration signals (g), measured at leading and trailing edges of the vertical tail tip section, were fed to the controller (Figure 3-7) to generate the electrical stimuli (u-volts) and to excite the actuators out-of-phase with the buffet load. A sub-optimal controller, based on the MATLAB Mu-analysis tools, was used in this study. The closed loop solutions, in terms of peak and rms values of accelerations and stresses, were computed.

Figures 4-30 and 4-31 compare tip accelerations of open loop and closed loop analyses. Similarly, Figure 4-32 contrasts the PSD (power spectral density) of the root stress computed for open and closed loop cases as a function of frequency in cycles per second (Hertz). The peak stress reduced from 6,696 psi (pounds per square inch) to 461 psi, while the rms (root mean square) stress reduced from 14,109 psi to 3,894 psi. The use of ACSM device shows a 72% reduction in the rms stress.

51
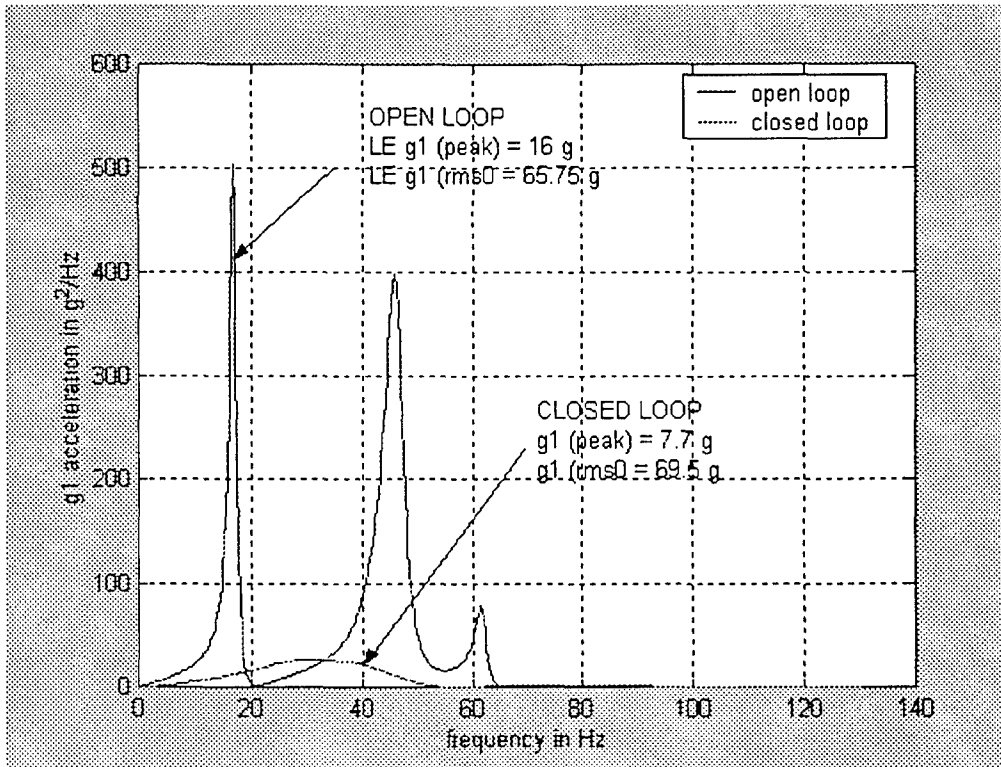
**Figure 4-30. Closed Loop Leading Edge Acceleration at 30k Altitude**
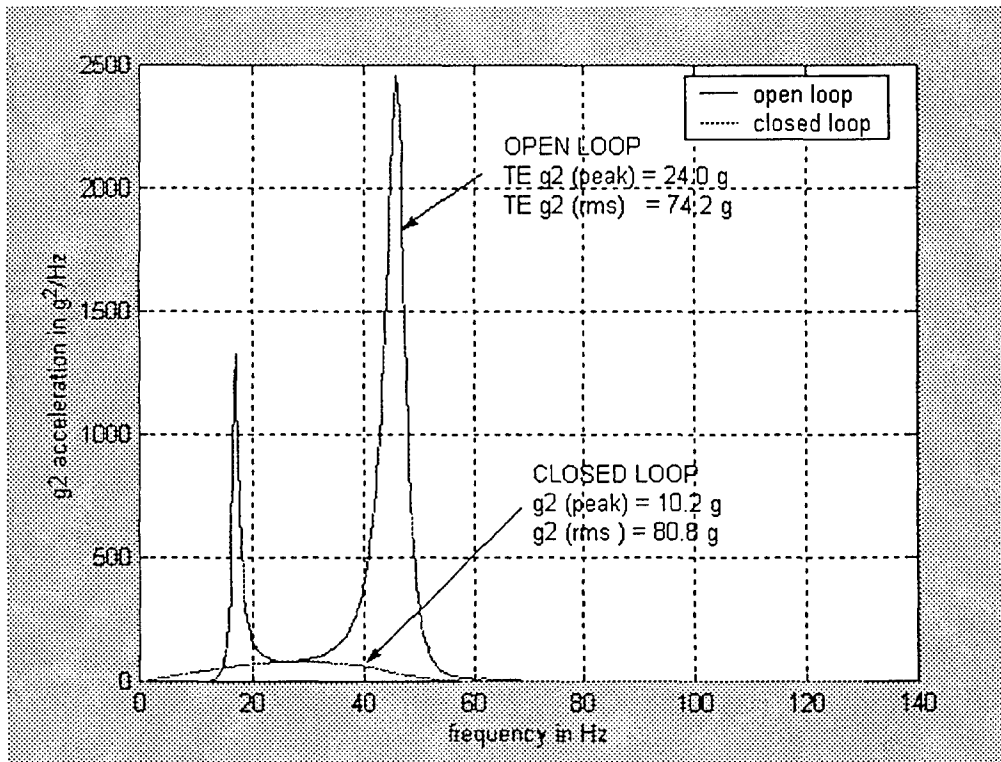
Figure 4-31. Closed Loop Trailing Edge Acceleration at 30k Altitude

52
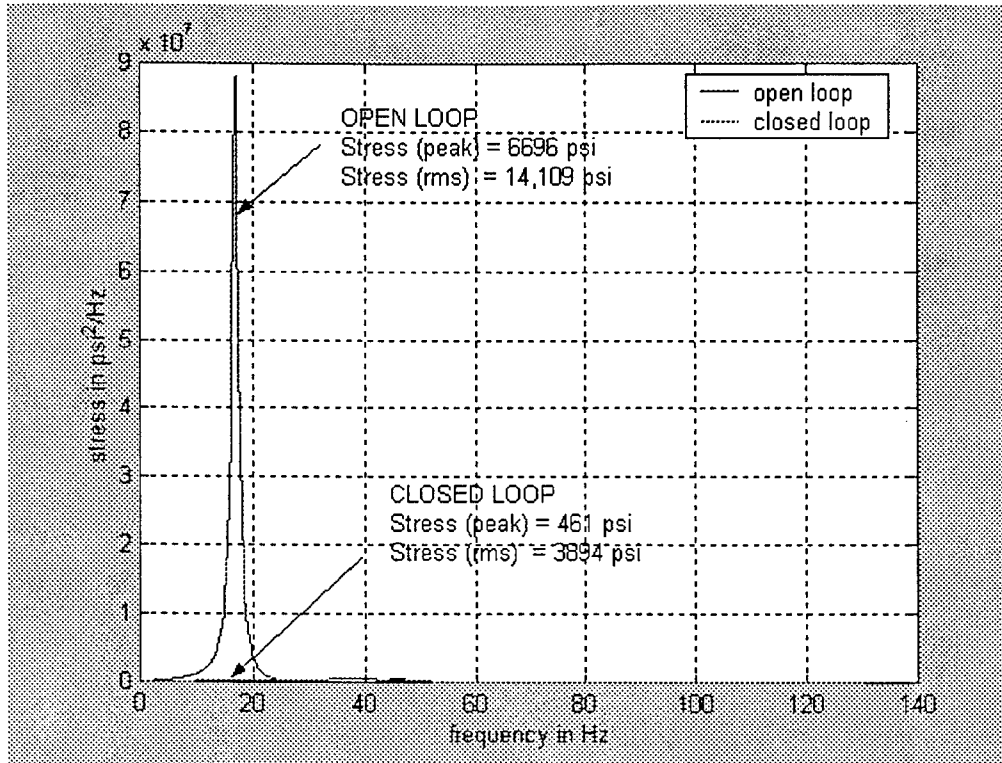
Figure 4-32. Closed Loop Root Stress PSD Due to Buffet Load; 30k altitude

4.5.3 Actuator Stimuli and Power

Figure 4-33 shows the electrical stimuli (in volt) applied to the piezoelectric actuators, u1, u2 and u3 used in this analysis. The average power required to drive an actuator is given by:

$$P_a = C.u_{max}u_{p-p}.f \qquad (4-1)$$

Maximum power for a sinusoidal operation is:

$$P_{max} = \pi P_a \qquad (4-2)$$

and:

$$C = n.\varepsilon_0\varepsilon_{33}(A/t_s) \qquad (4-3)$$

Where:

C = Actuator capacitance in Farad =amper.sec/volt

n = Number of layers

ε_0 = Dielectric constant in vacuum (amp.sec/volt.meter)

53

ε_{33} = Nondimensional relative dielectric constant

A = Surface area of the stack actuator

t_s = Thickness of the stack layer(= across individual electrodes)

u_{max} = Max amplifier voltage

u_{p-p} = Peak to peak drive voltage

f = Actuator working frequency. This is usually 1/3 the resonant frequency of the actuator.

The analysis used stack actuators, P-246.7, made by the Physik Instrumente (Ref. 18). The following data are used:

Max operating voltage	1000 v
Resonant frequency	3 kHz
Push/Pull Force	12500/2000 Newtons
Capacitance	3280 nF
Stiffness	200 N/μM
U_{p-p}	45, 94, and 156 volt (rms)

Assuming:

$$u_{max} = u_{p-p}/2.$$

For the piezoelectric actuators selected in the study, the peak-to-peak inputs were 44 volt, 94 volt and 156 volt.

The maximum power required to actuate the semi-span ACSM system is given by:

$$P_{max} = \pi(3280^{-09}).(45^2+94^2+156^2).3000/3 /2 = 182 \text{ watts}$$

Or, the average power required to actuate the active control device was:

$$P_a = 60 \text{ watts.}$$

The peak to peak voltage input was less than 160 V and the average power consumed was 60 watts, which is equivalent to a 60 watt house hold electric bulb. Thus, it appears the Active Control Surface Modal device can economically be installed into the rudder of F-18 aircraft to enhance the fatigue life of the vertical tail by a factor of 6 or more. Table 4-1 presents the summary of peak and rms values of accelerations and stresses for the 30000-ft. flight condition.
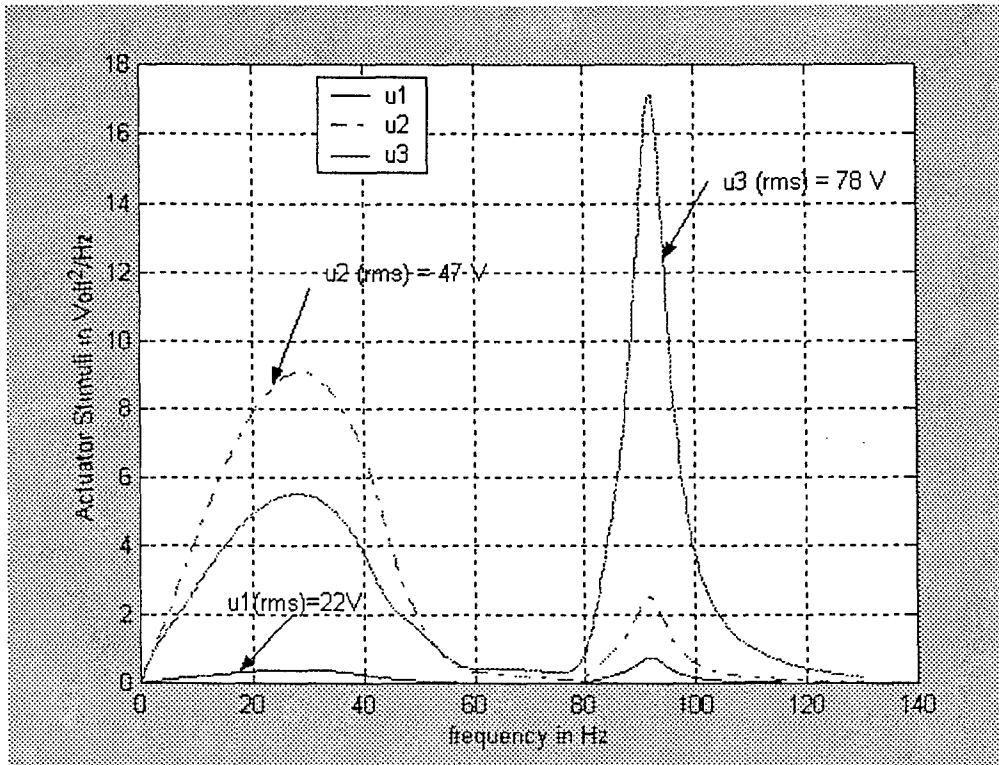
Fig 4-33 Actuator Input Stimuli in Volts for 30k altitude Flight Condition

Analysis	Open Loop Analysis		Closed Loop
	No Unsteady Aerodynamics	With Unsteady Aerodynamics	With Unsteady Aerodynamics
Peak L.E. Accel g_1	649.8 g	16.0 g	7.7 g
RMS g_1	86.4 g	65.75 g	69.5 g
Peak T.E. Accel g_2	969.8 g	239.0 g	10.2 g
RMS g_2	55.9 g	74.2 g	80.8 g
Peak Root Stress psi,	570,530.0 psi	6696.0 psi	461.0 psi
RMS stress	79,157.0 psi	14,109.0 psi	3,894.0 psi

Table 4-1. Summary of Stresses and Accelerations at 30,000 ft Altitude

4.5.4 Closed Loop Analysis at Sea Level

To study the impact of the dynamic pressure on aerodynamic damping and fatigue life, another set of analyses were performed at the sea level for the same configuration employed in the

55

previous case. The open loop and closed loop results of accelerations and stresses are presented in Figures 4-34, 4-35 and 4-36. The dynamic stress reduction was found to be 61%. Once again, this means a six-fold extension of the fatigue life. Figure 4-37 shows the PSD of the electrical stimuli applied across the actuator terminals. The RMS values of these stimuli were; u1 = 12.8 V, u2 = 22 V, and u3 = 32 V. The maximum power input was found to be a mere 21 watts. The reason for such low power input in contrast to the 30000-ft flight condition may be attributed to increased damping resulting from higher air density.

The summary of stress and acceleration is presented in Table 4-2. It is intriguing to note that the stresses at the 30k-altitude flight condition are higher than the corresponding values at the sea level flight condition. This is due to reduced damping at higher altitude.
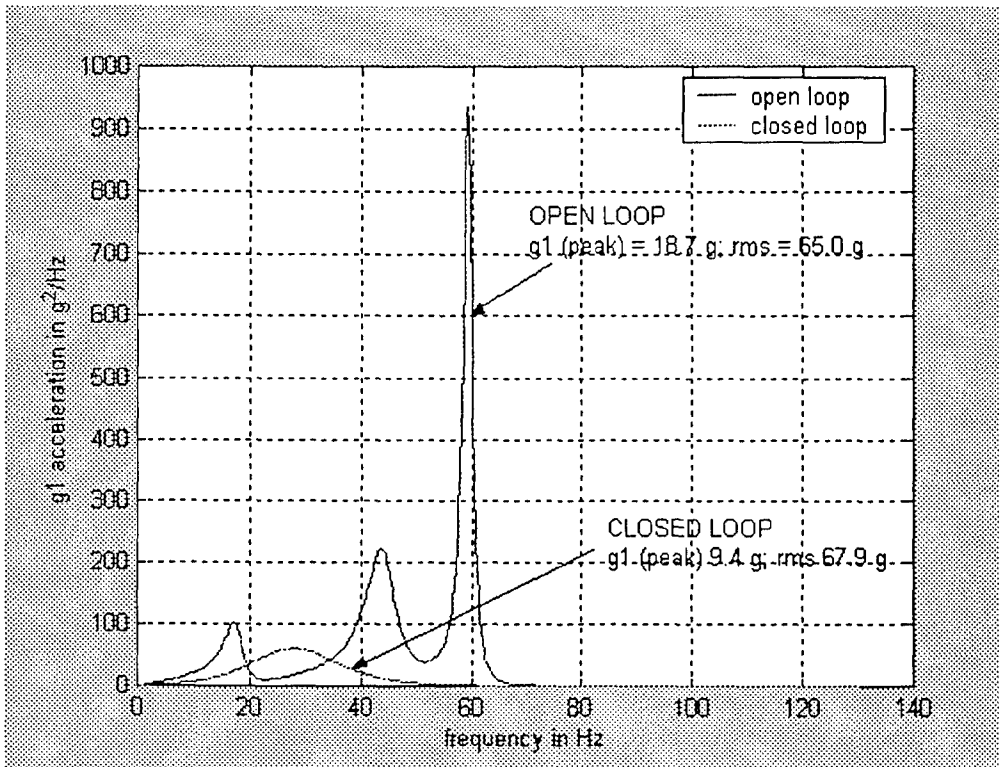

**Fig 4-34 Acceleration g_1 PSD in Sea Level Flight Condition**

56
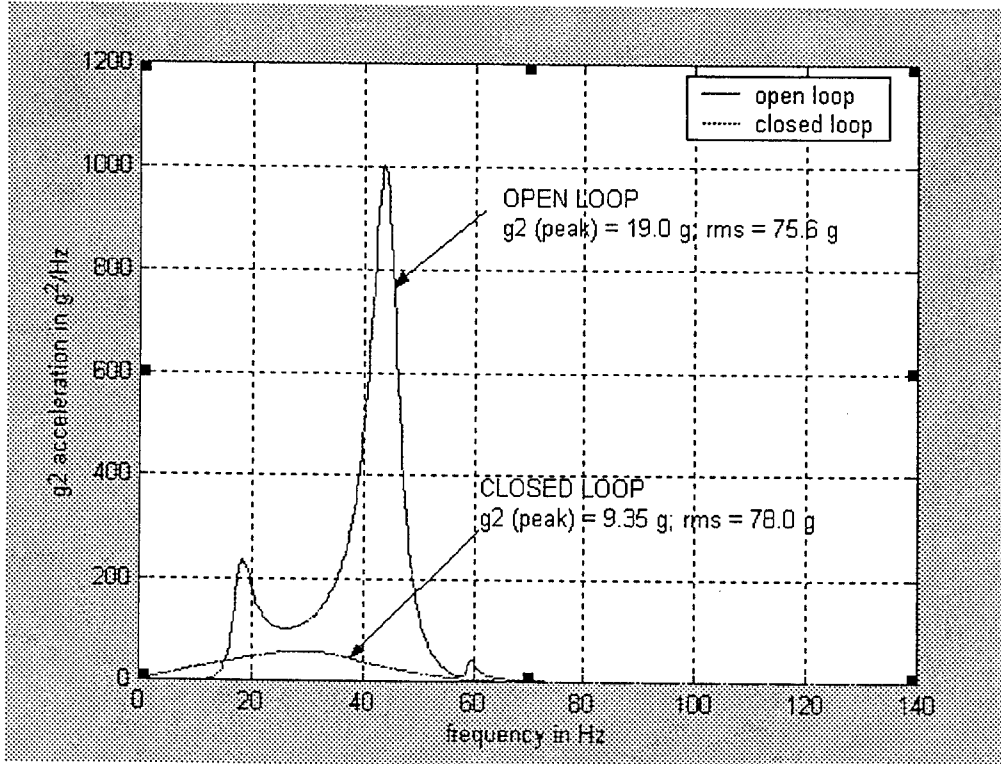
Fig 4-35 Acceleration g₂ PSD in Sea Level Flight Condition
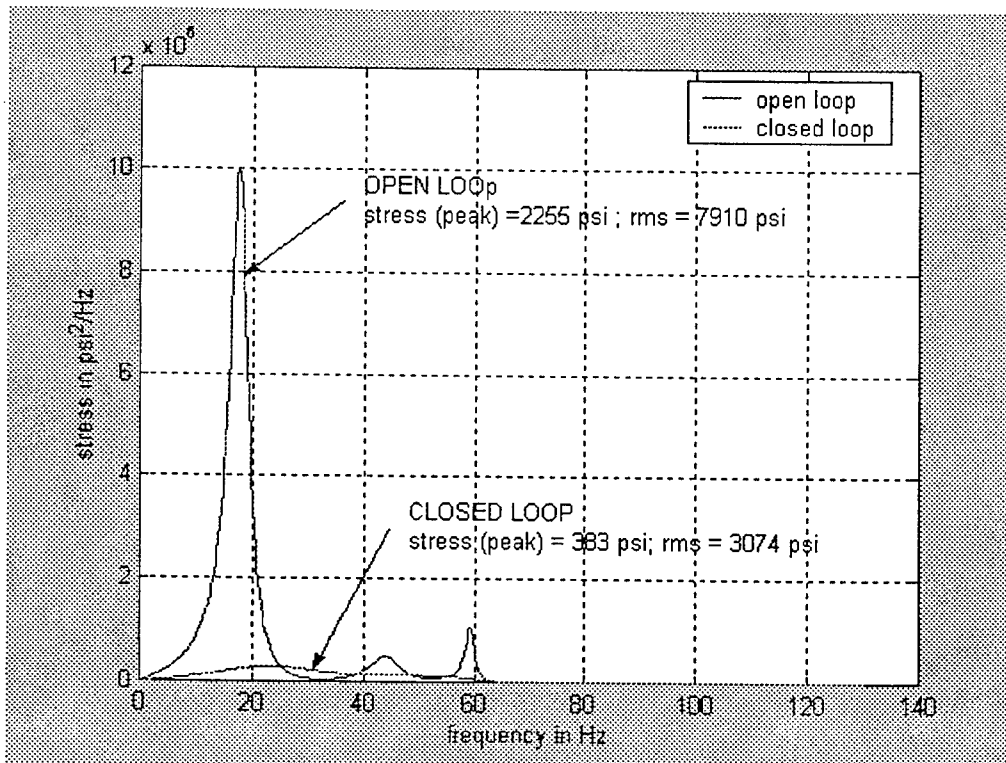

Fig 4-36 Stress PSD in Sea Level Flight Condition

57
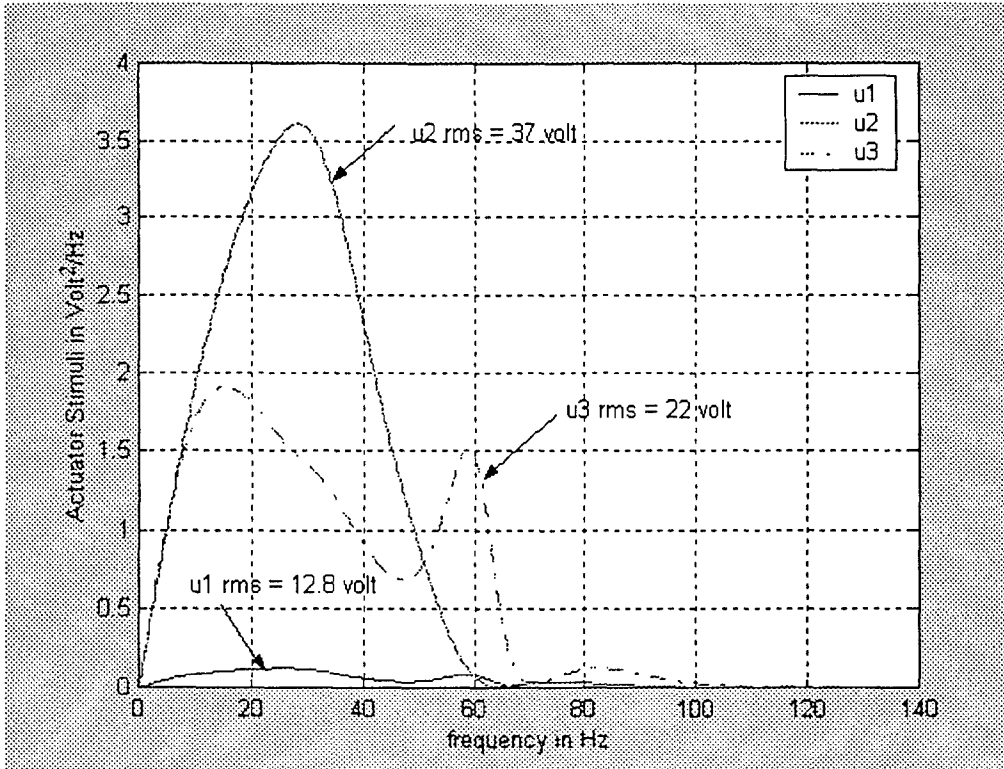
Fig 4-37 Actuator Input PSD in Sea Level Flight Condition

Analysis	Open Loop Analysis		Closed Loop
	No Unsteady Aerodynamics	With Unsteady Aerodynamics	With Unsteady Aerodynamics
Peak L.E. Accel g_1	649.8 g	131.86 g	35.5 g
RMS g_1	86.4 g	19.09 g	37.56 g
Peak T.E. Accel g_2	969.8 g	140.52 g	14.4 g
RMS g_2	55.9 g	92.68 g	66.67 g
Peak Root Stress psi,	570,530.0 psi	15,965.0 psi	924.8 psi
RMS stress	79,157.0 psi	9,239.0 psi	2,588.0 psi

Table 4-2. Summary of Stresses and Accelerations at Sea Level

4.5.5 Semi Span Active Control Surface Modal Device

The full span rudder active control surface modal device, in the previous example, yielded extremely good damping, which reduced the stress by a margin, more than necessary. Therefore, an investigation was made to determine whether a semi-span active control surface modal device was good enough to extend the fatigue life by a factor of two or three. Accordingly, the upper half of the rudder was selected and fitted with two actuators as depicted in Figure 4-38. Figure 4-39 shows the finite element modeling of the split rudder and the actuator placement at the semi-span location. The deformation mode of upper half of the rudder due to the actuator, u1 is shown in Figure 4-40. Similarly, the deformation pattern of the rudder due to the mid-span actuator, u2, is depicted in Figure 4-41. These two modes were used to generate the out-of-phase aerodynamic damping to reduce the buffet loads. The response analyses were performed using five vibration modes of the vertical tail and two active control surface modes. The frequencies of these modes in Hertz were:

Vibration Modes:,   16.23 Hz, 43.5 Hz, 49.2 Hz, 65.96 Hz, and 87.9 Hz.

Control Surface Modes: 297.9 Hz, and 173.0.Hz

The results of frequency response in terms of acceleration, stress and actuator input are presented next.
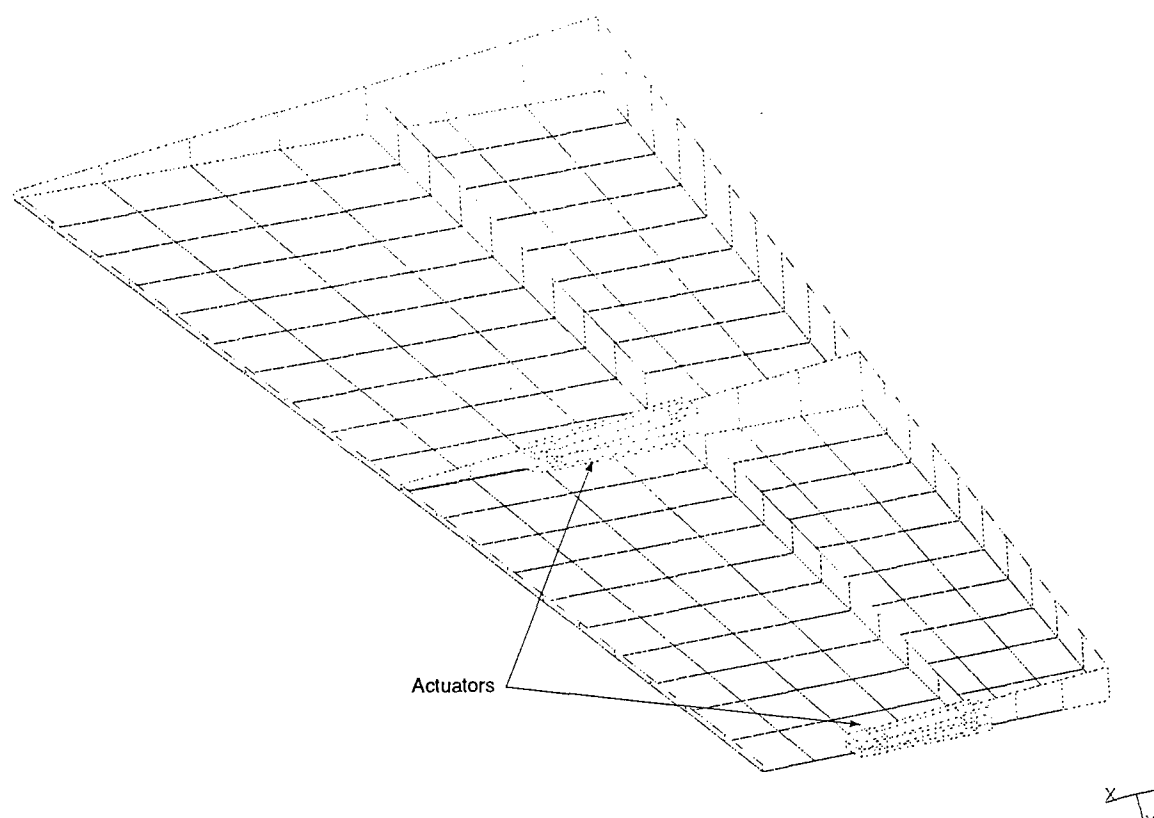

Actuators

Figure 4-38. Finite Element Rudder Model Showing Semi-Span Active Control Surface

Split in Rudder Trailing Edge
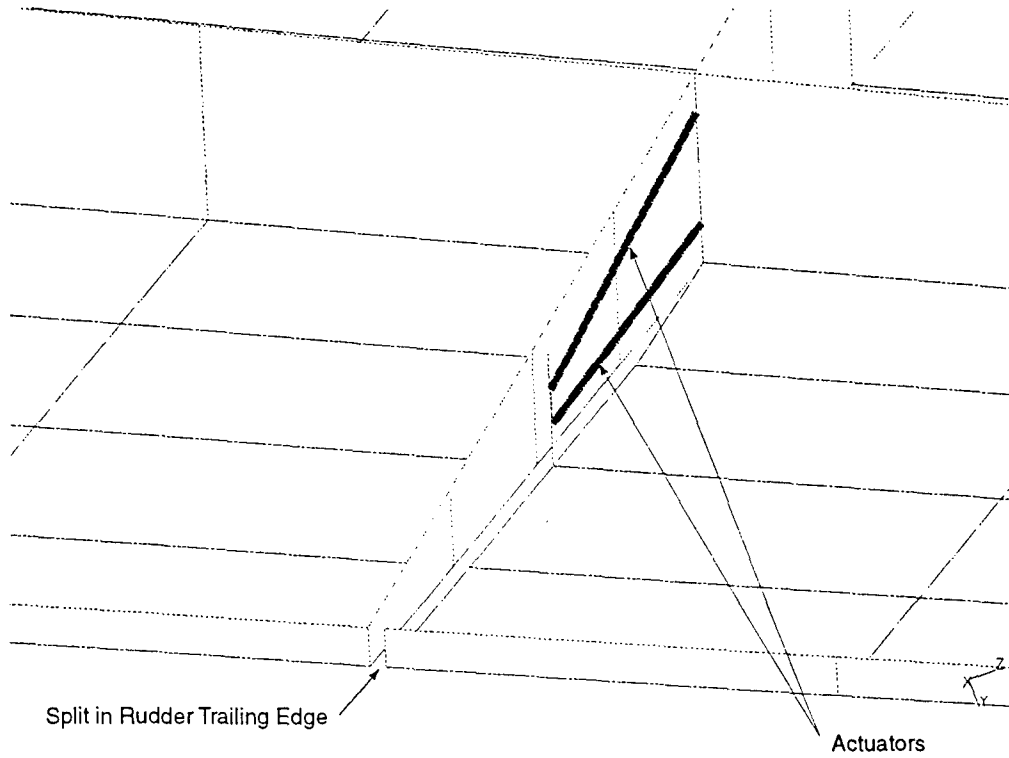
Actuators

Figure 4-39. Finite Element Model Showing Split Rudder and the Actuator Placement
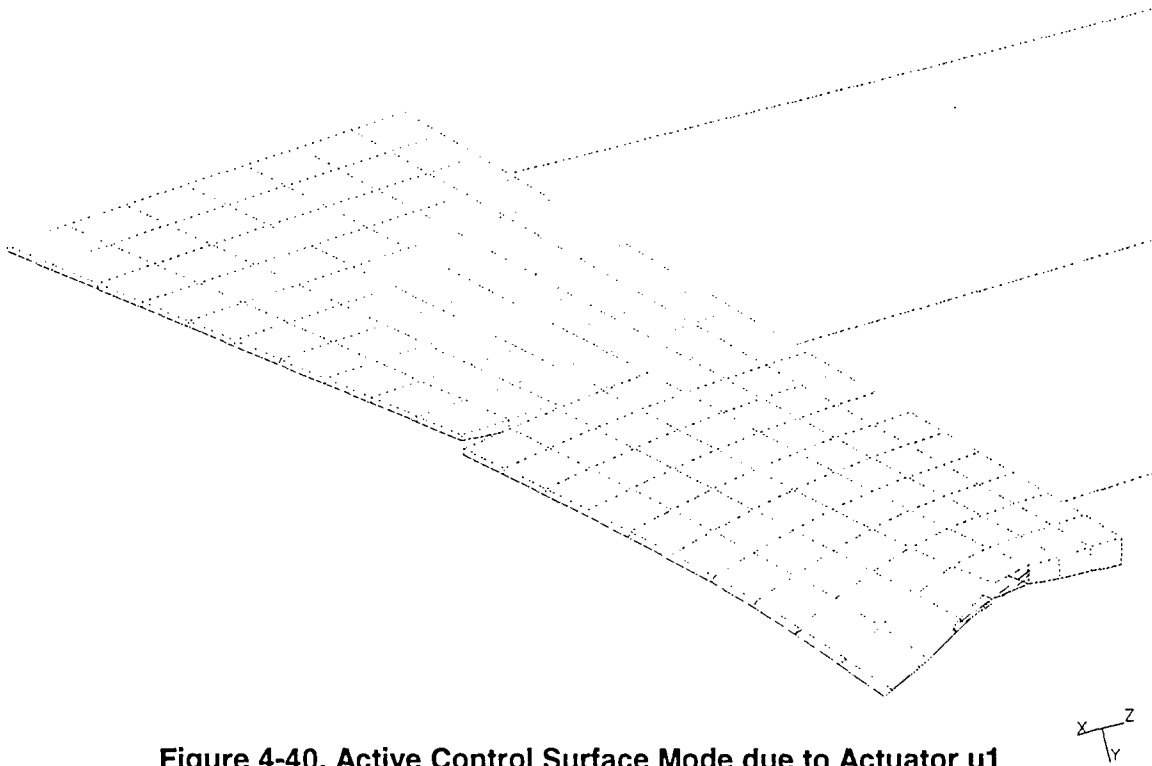

**Figure 4-40. Active Control Surface Mode due to Actuator u1**
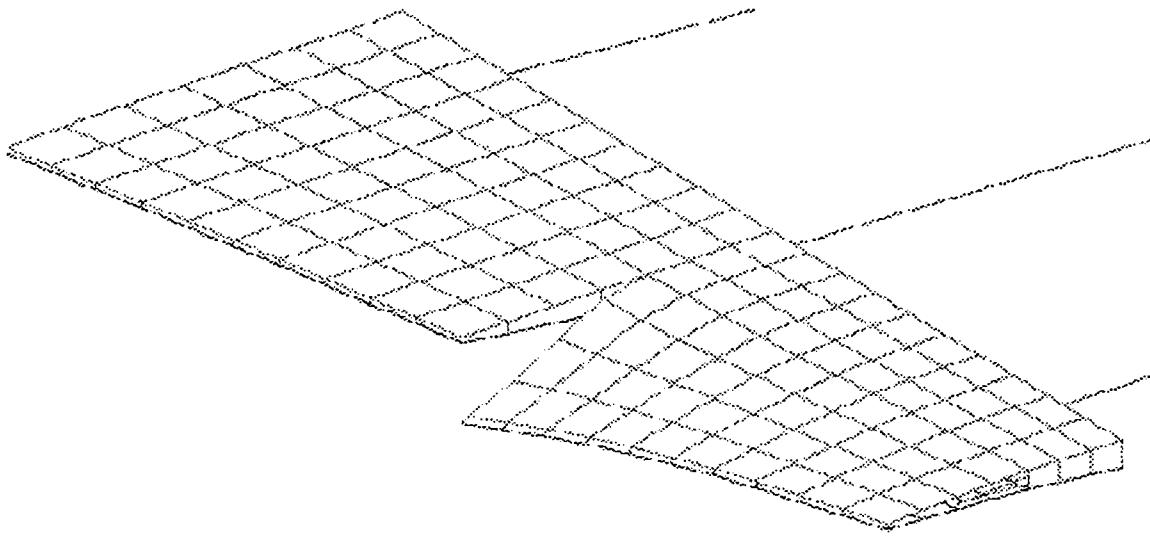
Figure 4-41. Active Control Surface Mode due to Actuator u2

The frequency response for acceleration, stress and actuator stimuli was computed for both open loop and closed loop analyses. These results are presented as power spectral density vs. frequency using linear and log scales for each data. The linear scale data highlights the relative magnitude of peak values of open loop and closed loop responses, while the log scale data shows the energy contained in the spectrum that relates to the root mean square (rms) value. Figure 4-42 show the vertical tail tip section leading edge acceleration (g1) psd. The peak acceleration, g1, reduces from 16 g to 10 g in the closed loop. Similar data for the trailing edge acceleration are shown in Figure 4-43 in which the peak acceleration, g2, reduces from 28 g to 13 g.
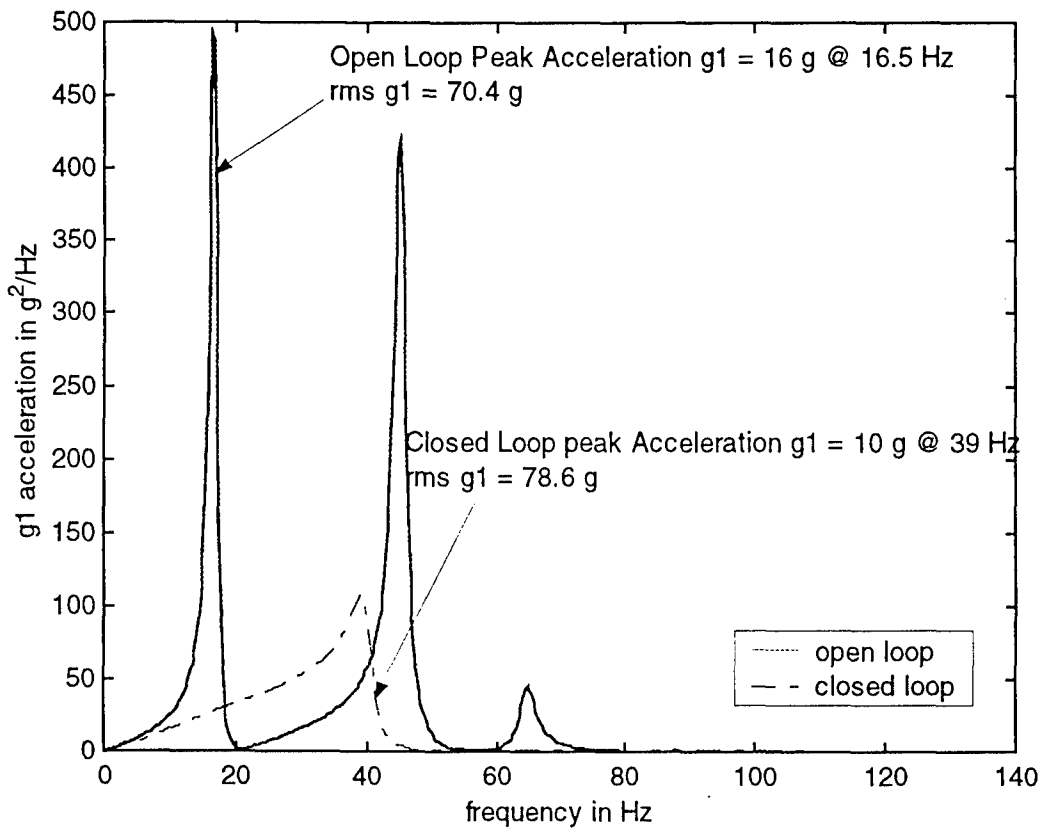
**Figure 4-42. Leading Edge Acceleration PSD g1 in Linear Scale**
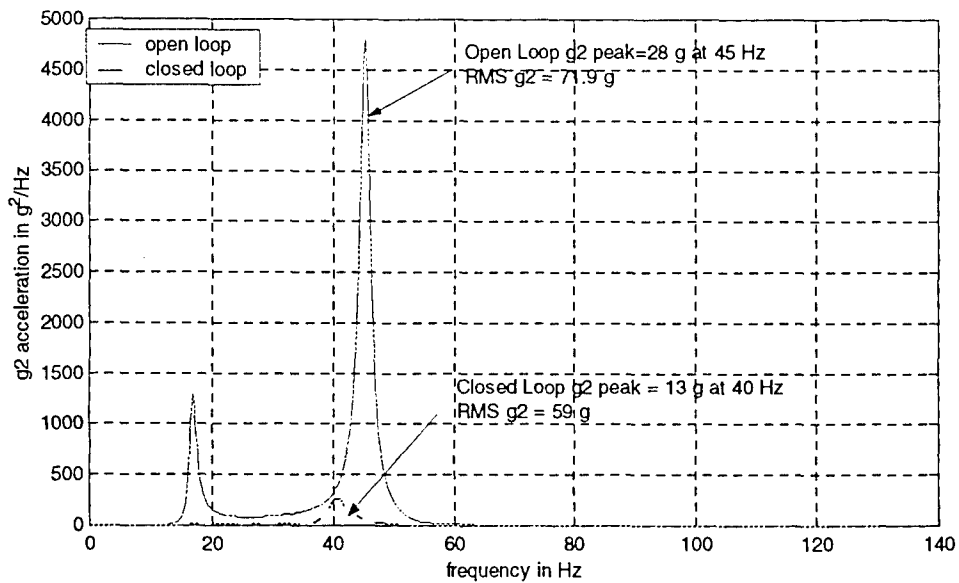
Figure 4-43. Trailing Edge Acceleration PSD g2 for the Semi-Rudder ACSM Device

Figure 4-44 presents the open loop and closed loop power spectral densities of the root stresses. The open loop peak stress reduces from 6969 psi to 1915 psi. Likewise, the open loop RMS stress reduces from 14,675 psi to 8598 psi. This amounts to 41% reduction as compared to 72% reduction for the full span rudder case. Hence, it appears the semi-span active rudder surface is sufficient to achieve desired fatigue life extension by a factor of four.

Figure 4-45 represents the power spectral densities of actuator input stimuli. For typical actuators selected in the study, the peak volt input for the top actuator is 24 volt, and 26 volt for the mid span actuator. The corresponding RMS input values are 108 v and 115 v respectively. The maximum power required to actuate the semi-span ACSM system is given by

$$P_{max} = \pi.3280^{-09}.(108^2+.115^2)\ 3.1000/3\ /2= 68\ watts$$

Or, the average power is given by:

$$P_a = 21\ watts$$

The maximum power is less than a 100 watt electric bulb.
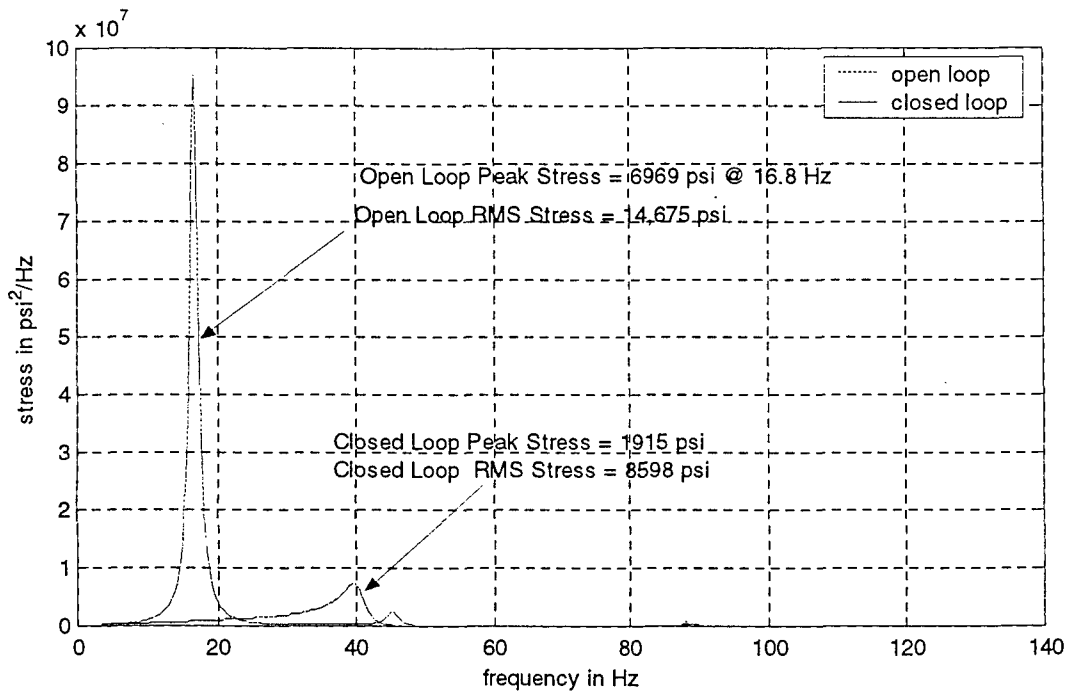
Figure 4-44. Vertical Tail Root Stress PSD for the Semi-Rudder ACSM Device
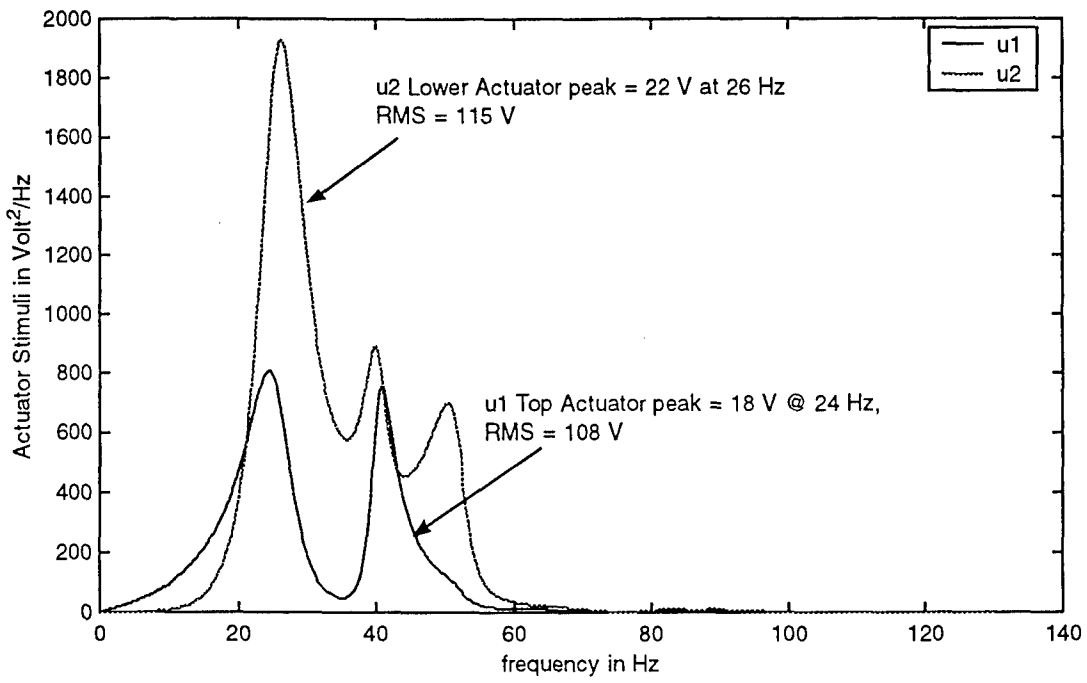
Figure 4-45. Actuator Stimuli (Volts) for the Semi-Rudder ACSM Device

5 CONCLUSIONS AND RECOMMENDATIONS

These analyses prove that the proposed concept is feasible and that the fatigue life of critical components of the vertical tail can be significantly increased. This improvement could save the US Government and commercial airline operators millions of dollars per aircraft during its service life. The preliminary results are very encouraging and suggest that further evaluation of the concept in actual flight conditions should be continued so that the technology can be soon transitioned into practice.

In general, the fatigue life of a metallic structure increases by one lifetime for every 10% reduction in the RMS stress. Accordingly, this example shows eight-fold increase in the fatigue life. Thus, the active control surface modal device has proved to be very effective in reducing the dynamic effects. Similar, trends have been observed in the case of the gust environment. Likewise, flutter suppression can also be achieved with great success.

From all of the foregoing, consider some of the advantages of the proposed active control surface modal device over the known flutter suppression and load alleviation methods:

1. These innovations are expected to provide overwhelming aerodynamic damping in a wide-band frequency spectrum so that buffet, gust and flutter associated dynamic problems can be attended to by means a single ACSM device.

2. An independent active control algorithm is provided so that there is no interference with the flight control system, which the pilots like the most.

3. The modified control surface preserves all of the entities of a conventional control surface, since it is able to rotate about the hinge line, and fulfill the requirements of directional control of an aircraft.

4. The proposed device can be retrofitted to existing aircraft very economically, and can also be implemented into new aircraft still more economically.

5. It should be understood that the foregoing description is only illustrative of the invention. Various alternatives and modifications can be devised by those skilled in the art without departing from the invention. Accordingly, the present invention is intended to embrace all such alterations, modifications and variances that fall within the scope of the appended claims.

6. The proposed device can very conveniently be fitted on to a flight test vehicle and be demonstrated the proof of concept for flutter suppression and buffet/gust load alleviation missions.

7. This could save millions of dollars per aircraft in reduced repair cost, reduced down time cost, and increased readiness of existing fleet of aircraft.

6 REFERENCES

1. Moses, R. W., "Active Vertical Tail Buffeting Alleviation on a Twin-Tail Fighter Configuration in a Wind Tunnel," presented at the CEAS International Forum on Aeroelasticity and Structural Dynamics 1997, 17-20 June 1997, Rome, Italy.

2. Patel, S. R., "Empennage Dynamic Buffet Loads," briefing by Lockhead-Boeing F-22 Structures A & I Team, March 19, 1993.

3. Meyn, L. A., and James, K. D., "Full-Scale Wind Tunnel Studies of F/A –18 Tail Buffet," Journal of Aircraft, Vol. 33, N0.3, May-June 1996.

4. Shah, G. H., "Wind Tunnel Investigation of Aerodynamic and Tail Buffet Characteristics of Leading Edge Extension Modifications to the F/A –18," AIAA paper 91-2889, Aug. 1991.

5. Bean, D. E., and Wood, N. J., "An Experimental Investigation of Twin Fin Buffeting and Suppression," AIAA-93-0054, presented at 31st Aerospace Sciences Meeting, Reno NV, Jan. 1993.

6. Ashley, H., Rock, S. M., Digumathi, R., Chaney, K., and Rggers, Jr., A. J., "Active Control For Fin Buffet Alleviation," WL-TR-93-3099, January, 1994, Flight Dynamics Directorate, Wright Laboratory, Air Force Materiel Command, Wright-Patterson Air Force Base, OH 45433-7562.

7. Moses, R. W., and Ashley, H., "Spatial Characteristics of the Unsteady Differential Pressures on 16% F/A-18 vertical tails," 36th AIAA Aerospace Sciences Meeting and Exhibit, Reno, Nevada, January 12-15, 1998.

8. Barrett, R., "Advanced Low-Cost Smart Missile Fin Technology Evaluation," December 1993, Sponsored by the United States Air Force, Wright Laboratory, Armament Directorate, Eglin AFB, FL.

9. Moses, R. W., "Vertical Tail Buffeting Alleviation Using Piezoelectric Actuators-Some Results of the Actively Controlled Response of Buffet-Affected Tails (ACROBAT)," NASA TM 110336, April 1997, NASA Langley Research Center, Hampton , Virginia.

10. Yurkovich, R., "Prediction of Tail Buffet Loads for Design Applications," presented to the Aerospace Flutter and Dynamics Council, 29 October 1987.

11. Zimmerman, N. H., and Ferman, M. A., "Prediction of Tail Buffet Loads for Design Application," Vols. I and II, Report No. NADC-88043-60, Jul7 1987.

12. Sheta, E. F., Harrand, V. J., and Huttsell, L. J., "Active Vortical Flow Control For Alleviation of Twin-Tail Buffet of Generic Fighter Aircraft," Paper No. AIAA 2000-0906, AIAA 38th Aerospace Sciences Meeting and Exhibit, January 10-13, 2000, Reno, NV.

13. Lind, R., and Brenner, M., *Robust Aeroservoelastic Stability Analysis,* Advances in Industrial Control, Springer, 1999

14. Appa, K., Ausman, J., and Khot, N. S., "Smart Actuation Systems For Enhanced Aircraft Maneuver Performance," Flight Dynamics Directorate, AFRL-VA-WP-TR-1999-3047, October 1998.

15. Appa, K., Ausman, J., and Khot, N. S., Feasibility Assessment and Optimization of Smart Actuation Systems for Enhanced Aircraft Maneuver Performance, Flight Dynamics Directorate, WL-TR-97-3083, July 1997.

16. Johnson, E. H., and Venkayya,V. B., Automated Structural Optimization System (ASTROS), Volume I – Theoretical Manual, Flight Dynamics Laboratory, Air Force Wright Aeronautical Laboratories, Wright-Patterson Air Force Base, Ohio 45433-6553, December, 1988.

17. Anon, MATLAB, The Language of Technical Computing, Version V, The Mathworks Inc., 1999.

18. Anon, Mu-Analysis and Synthesis Toolbox, Version 3. , The Mathworks Inc., 1999.

19. Zhou, K., and Doyle, J. C., Essentials of Robust Control, Prentice Hall, Upper Saddle River, New Jersey 07458, 1998.